J. Fluid Mech. (2005), *vol.* 532, *pp.* 63–109.
doi:10.1017/S0022112005003836 Printed in the United Kingdom

Receptivity of a supersonic boundary layer over a flat plate. Part 3. Effects of different types of free-stream disturbances

By YANBAO MA AND XIAOLIN ZHONG

Mechanical and Aerospace Engineering Department, University of California, Los Angeles, CA 90095, USA

(Received 11 November 2003 and in revised form 7 December 2004)

Supersonic boundary-layer receptivity to different types of free-stream disturbance is studied for a Mach 4.5 boundary-layer flow over a flat plate by using the approaches of both direct numerical simulation and linear stability theory. This paper is Part 3 of a three-part study of the receptivity of supersonic boundary layers to free-stream disturbances. The present paper investigates receptivity to four types of different free-stream disturbances, i.e. slow and fast acoustic waves, entropy waves, and vorticity waves. A high-order shock-fitting scheme is used in the numerical simulation in order to accurately account for the effects of interactions between free-stream disturbance waves and the oblique shock wave. Numerical results on the generation of fast acoustic waves by free-stream entropy waves or vorticity waves are compared with those of a linear theory. Good agreement is obtained in both wave angles and amplitudes immediately behind the bow shock. It is found that the second-mode receptivity to free-stream slow acoustic waves is several times stronger than that to free-stream fast acoustic waves. This is because free-stream slow acoustic waves can directly induce and interact with the first and second Mack modes, while free-stream fast acoustic waves cannot. Instead, the free-stream fast acoustic waves can only induce and interact with stable mode I waves, which in turn induce unstable Mack modes. In the cases of receptivity to free-stream entropy waves and vorticity waves, it is found that the oblique shock wave created by the displacement of the boundary layer plays an important role because boundary-layer disturbances are mainly induced by fast acoustic waves generated behind the shock by free-stream forcing waves. As a result, mechanisms of the receptivity to free-stream entropy and vorticity waves are very similar to those of the receptivity to free-stream fast acoustic waves.

1. Introduction

Laminar–turbulent transition of hypersonic boundary layers can significantly affect skin friction and surface heating rates because turbulent flow generates much higher shear forces and heating rates. Thus, the accurate prediction of boundary-layer transition is a critical part of the design of the thermal protection systems of hypersonic vehicles. In general, the transition is a result of the nonlinear response of laminar boundary layers to forcing environmental disturbances (Herbert & Morkovin 1979; Morkovin 1989; Reshotko 1994; Herbert 1996). Depending on the amplitudes of forcing disturbances, there are several transition scenarios based on the 'roadmaps' of transition to turbulence for boundary layers in external flows as described by Nishioka & Morkovin (1986) and Saric, Reed & Kerschen (2002). Receptivity is the

first stage of a transition process. In the receptivity process, forcing disturbances enter a boundary layer as perturbations of the basic state (Morkovin 1969; Reshotko 1984). The perturbations caused by the forcing waves provide important initial conditions for amplitudes, frequencies, and phases of instability waves which grow in the boundary layer and eventually lead to transition. In an environment with small initial disturbances, the second stage is the generation and development of primary boundary-layer instability wave modes, which are followed by secondary instabilities and nonlinear breakdown to turbulence. For supersonic and hypersonic vehicles in flight, the initial amplitudes of environmental disturbances are generally very small. Under such conditions, the transition is likely to be the result of a growth of primary boundary-layer instability modes, which are generated by a receptivity process. Currently, the receptivity mechanisms for generation of the primary boundary-layer modes in supersonic and hypersonic boundary layers are not well understood and remain an important area of current research.

Receptivity of low-speed incompressible boundary-layer flows has been extensively studied in the last three decades (Saric *et al.* 2002). However, there have been only a few theoretical, computational or experimental studies on the receptivity of compressible boundary layers (Ma & Zhong 2003*b*). Fedorov (1997), Fedorov & Khokhlov (2001, 2002) and Fedorov & Tumin (2001) showed that the receptivity mechanisms of supersonic and hypersonic boundary-layer flows are essentially different from those of subsonic and relatively low supersonic flows. Specifically, they found three new features associated with the receptivity of supersonic boundary-layer flow. First, two boundary-layer wave modes, which were termed modes 1 and 2, can be synchronized with the fast and slow acoustic waves of non-dimensional phase speeds $1+1/M_e$ and $1-1/M_e$ in the leading-edge region, respectively. Secondly, mode 1 can be synchronized with external entropy/vorticity waves with a phase speed equal to free-stream velocity. Thirdly, there is a synchronization point between mode 1 and 2 near branch I of the second-mode neutral stability point. Based on the first feature, they predicted that modes 1 and 2 can be effectively excited by acoustic waves near the leading-edge region, in qualitative agreement with the leading-edge receptivity experiment of a Mach 6 flow over a flat plate by Maslov *et al.* (2001). Furthermore, Fedorov and colleagues showed that there is an intermodal exchange due to a wave-mode synchronization between mode 1 and mode 2. After the synchronization, one of the two modes converts to the second Mack mode.

The characteristics of supersonic boundary-layer normal modes were studied in Part 1 of this series (Ma & Zhong 2003*a*). It was found that the well-accepted first, second and third modes are, in fact, different sections of a single mode (see figure 7 in Ma & Zhong 2003*a*). These single modes were simply called Mack modes for convenience of discussion. Ma & Zhong also found a family of stable wave modes in the supersonic boundary layer. These stable modes were termed mode I, mode II, mode III, etc. Mode I was called mode 1 and the first Mack mode was called mode 2 in Fedorov & Khokhlov (2001).

The main features of the supersonic boundary-layer normal modes analysed by Fedorov *et al.* were in qualitative agreement with our numerical simulation (Ma & Zhong 2003*a*, *b*). It was shown in Ma & Zhong (2003*a*) that both mode I and the first Mack mode can convert to the unstable Mack second mode in numerical simulations. Although mode I and mode II waves are always stable, they can have direct resonant interactions with both the fast acoustic waves and the Mack-mode waves. The generation of mode I waves by free-stream fast acoustic waves and the conversion of mode I waves to the Mack second-mode waves were verified in Ma &

Zhong (2003*b*), where the receptivity of Mach 4.5 flow over a flat plate to free-stream fast acoustic waves was studied using DNS. It was shown that the receptivity leads to the excitation of both Mack modes and a family of stable modes, i.e. mode I, mode II, etc. The forcing fast acoustic waves do not interact directly with the unstable Mack second mode. Instead, the stable mode I waves interact with both the fast acoustic waves near the leading edge and the unstable Mack-mode waves downstream. Through this two-step interaction process, the stable mode I waves transfer wave energy from the forcing fast acoustic waves to the second Mack-mode waves inside the boundary layer. In Fedorov & Khokhlov (2001), it was also predicted that mode 2 (the traditional first mode) can be directly generated by free-stream slow acoustic waves in the leading-edge region, and mode 1 (mode I in Ma & Zhong 2003*a*) can be effectively excited by vorticity waves and entropy waves, which are synchronized with mode 1, after vorticity waves and entropy waves are swallowed by the boundary layer. These two theoretical predictions have not yet been verified. In addition, boundary-layer self-similar solutions were used in Fedorov's analyses, so the effect of the bow shock wave on the receptivity process was not considered.

Before entering the boundary layer, free-stream disturbances first pass through and interact with an oblique shock created by the boundary-layer displacement. According to the linear analyses of Ribner (1954), McKenzie & Westphal (1968) and Anyiwo & Bushnell (1982), the interaction between free-stream disturbances and the oblique shock generates all three kinds of transmitted disturbance waves, i.e. acoustic waves, vorticity waves and entropy waves, irrespective of the nature of the free-stream disturbance waves. These three kinds of transmitted waves propagate downstream and interact with the boundary layer on the flat plate. Meanwhile, the perturbed boundary layer also generates reflected acoustic waves propagating back to the shock. When the reflected acoustic waves impinge on the shock, the interaction generates additional reflected disturbances of all three kinds of waves, which in turn propagate downstream. The combined effects of the interactions between the oblique shock and the free-stream disturbances as well as the reflected acoustic waves from the wall can have strong effects on the receptivity process of the supersonic boundary layer behind the shock.

Therefore, the objective of this paper is to study the receptivity mechanisms of a Mach 4.5 supersonic boundary layer to free-stream slow acoustic waves, entropy waves and vorticity waves, by numerical simulations. Especially, it aims to verify the theoretical prediction of Fedorov & Khokhlov (2001) on the generation of the first mode by slow acoustic waves in the leading-edge region, and excitation of mode I by entropy/vorticity waves at the resonant point downstream. The results of different types of free-stream disturbances on boundary-layer receptivity are also compared with previous receptivity results for free-stream fast acoustic waves. In the numerical simulations, the forcing free-stream slow acoustic waves, entropy waves and vorticity waves are superimposed on the steady base flow in front of the shock. The subsequent interaction of the forcing waves with the shock and the excitation of boundary-layer wave modes are numerically simulated by computing the full Navier–Stokes equations. The receptivity properties are analysed based on the results of the numerical simulations and by linear stability analyses. The effects of the incident wave angles and the frequencies of the forcing waves are also studied.

2. Governing equations and numerical methods

The governing equations and numerical methods have been described in detail in Parts 1 and 2 (Ma & Zhong 2003*a*, *b*). The supersonic air flow is assumed to be

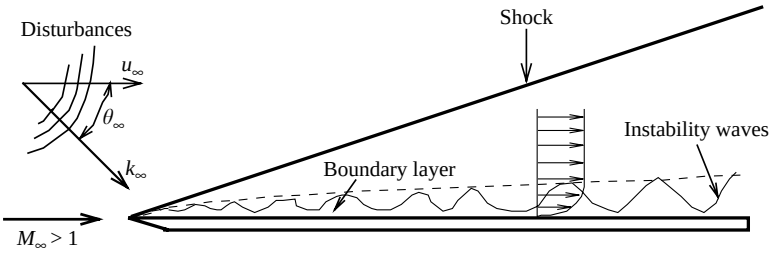

FIGURE 1. A schematic of the receptivity to free-stream disturbances for a supersonic boundary layer over a flat plate.

a thermally and calorically perfect gas. The governing equations in the numerical simulations are the two-dimensional full Navier–Stokes equations, which can be written in conservative form as follows:

$$\frac{\partial \boldsymbol{U}^*}{\partial t^*} + \frac{\partial}{\partial x^*}(\boldsymbol{F}_1^* + \boldsymbol{F}_{v1}^*) + \frac{\partial}{\partial y^*}(\boldsymbol{F}_2^* + \boldsymbol{F}_{v2}^*) = 0, \tag{1}$$

where the superscript '*' represents dimensional variables, $\boldsymbol{U}^*$ is a vector containing the conservative variables, $\{\rho^*, \rho^* u^*, \rho^* v^*, e^*\}$, $\boldsymbol{F}_1^*$ and $\boldsymbol{F}_2^*$ are inviscid flux vectors, and $\boldsymbol{F}_{v1}^*$ and $\boldsymbol{F}_{v2}^*$ are viscous flux vectors. Unless stated otherwise, dimensional flow variables in this paper are non-dimensionalized by using the steady-state free-stream conditions. Specifically, velocities are non-dimensionalized by the free-stream velocity u_∞^*, length scales by a boundary-layer thickness length L^* given by (4) in the next section, density by ρ_∞^*, pressure by p_∞^*, temperature by T_∞^*, time by L^*/u_∞^*, vorticity by u_∞^*/L^*, entropy by c_p^*, wavenumber by $1/L^*$, circular frequency by u_∞^*/L^*, etc. The dimensionless flow variables are denoted by the same notations as their dimensional counterparts, but without the asterisk.

The fifth-order shock-fitting finite-difference method of Zhong (1998) is used to compute the two-dimensional nonlinear Navier–Stokes equations in the unsteady flow fields bounded by the bow shock and the flat plate (figure 1). The shock-fitting method treats the unsteady bow shock as a computational boundary which is oscillatory because of its interaction with the free-stream forcing waves and with the reflected waves from the wall surface. The flow variables behind the unsteady shock are determined by the Rankine–Hugoniot relations across the shock, coupled with a characteristic compatibility equation from behind the shock. The transient movement of the shock and its interaction with free-stream disturbance waves are solved as a part of the numerical simulation solutions. The use of the shock-fitting method makes it possible to use high-order finite-difference schemes for spatial discretization of the Navier–Stokes equations. A fifth-order upwind finite-difference scheme is applied for the convective terms while a sixth-order central difference scheme is used for the discretization of the viscous terms. The spatial discretization of the governing equations leads to a system of first-order ordinary differential equations. A first-order explicit Runge–Kutta (RK) method is used for the temporal integration because the time step was very small in transient viscous flow simulations. We have calculated the same case with the third-order RK integration. Almost identical results are obtained to those from the first order. Therefore, the first-order RK integration is used in our study.

The non-slip boundary condition is used for velocity at the wall. An adiabatic wall-boundary condition is used for the steady base flow. For unsteady-flow simulations,

temperature perturbations on the wall are set to be zero. The use of zero temperature perturbation boundary conditions for an adiabatic mean flow is consistent with all other theoretical analyses and linear stability theory (LST) calculations.

3. Flow conditions

The flow conditions are the same as those used in Kendall's (1975) experiment on the stability of a Mach 4.5 boundary-layer flow over a flat plate, i.e.

$$M_\infty = 4.5, \qquad T^*_\infty = 65.15\,\mathrm{K},$$
$$p^*_\infty = 728.44\,\mathrm{Pa}, \qquad Pr = 0.72,$$

Free-stream unit Reynolds number: $Re^*_\infty = \dfrac{\rho^*_\infty U^*_\infty}{\mu^*_\infty} = 7.2 \times 10^6\,\mathrm{m}^{-1}$.

In many figures in this paper, the results are plotted as functions of the dimensional x^*-coordinate along the flat plate because this test case has been studied by Kendall (1975). The dimensional x^*-coordinate in the figures can be easily converted to dimensionless local Reynolds numbers by means of the following formula:

$$Re_x = Re^*_\infty x^* = 7.2 \times 10^6\,\mathrm{m}^{-1} x^*, \tag{2}$$

where x^* is the dimensional coordinate in metres measured from the leading edge along the plate surface.

In studies of boundary-layer stability, the Reynolds number is often taken as

$$R = \frac{\rho^*_\infty u^*_\infty L^*}{\mu^*_\infty}, \tag{3}$$

where

$$L^* = \sqrt{\frac{\mu^*_\infty x^*}{\rho^*_\infty u^*_\infty}}. \tag{4}$$

Hence, the relation between R and the local Reynolds number Re_x is

$$R = \sqrt{Re_x}. \tag{5}$$

In terms of R, the full computational domain of the current simulations spans from $R = 207.9$ to $R = 2129.8$. The inflow conditions at $R = 207.9$ are given by numerical solutions from total variation diminishing (TVD) methods. The calculation of steady base flow is described in detail in Ma & Zhong (2003*a*). In the actual simulations, the computational domain is divided into 11 sub-zones with a total of 3121 grid points in the streamwise direction and 121 grid points in the wall-normal direction. A grid-stretching function is used in the wall-normal direction to cluster more points inside the boundary layer near the wall. The grid points are distributed uniformly in the streamwise direction. The numerical accuracy of the results based on this grid assignment has been evaluated by grid refinement studies to ensure the grid independence of the numerical solutions (Ma & Zhong 2001).

4. Free-stream disturbances

The wave fields are represented by perturbations in the following form,

$$q'(x, y, t) = q(x, y, t) - \bar{q}(x, y), \tag{6}$$

where $q'(x, y, t)$ represents the perturbation of any flow variable, $q(x, y, t)$ is the instantaneous value obtained by an unsteady numerical simulation of the nonlinear Navier–Stokes equations, and $\bar{q}(x, y)$ is the steady component obtained by a separate steady-flow simulation of the Navier–Stokes equations. The effects of the interactions between the oblique shock and the free-stream disturbances are accurately taken into account by using the high-order shock-fitting method. In the simulations, the free-stream disturbances are superimposed on the steady base flow to investigate the excitation and development of boundary-layer instability waves. Before reaching the shock, the free-stream forcing disturbances are assumed to be weak monochromatic planar acoustic, entropy or vorticity waves.

For weak free-stream disturbances, the perturbations of an arbitrary flow variable can be written in the following form:

$$\begin{Bmatrix} u' \\ v' \\ p' \\ \rho' \end{Bmatrix}_{\infty} = \begin{Bmatrix} |u'| \\ |v'| \\ |p'| \\ |\rho'| \end{Bmatrix}_{\infty} \exp(\mathrm{i}[k_x x + k_y y - \omega t]), \tag{7}$$

where $|u'|$, $|v'|$, $|p'|$ and $|\rho'|$ are dimensionless free-stream perturbation amplitudes satisfying the following relations for the four types of linear waves:
fast acoustic waves $[\omega = k_\infty(1/M_\infty + \cos\theta_\infty)]$:

$$\begin{aligned} |u'|_\infty &= \epsilon\cos\theta_\infty, \quad |v'|_\infty = -\epsilon\sin\theta_\infty, \\ |p'|_\infty &= \epsilon\gamma M_\infty, \qquad |\rho'|_\infty = |p'|/\gamma; \end{aligned} \tag{8}$$

slow acoustic waves $[\omega = k_\infty(-1/M_\infty + \cos\theta_\infty)]$:

$$\begin{aligned} |u'|_\infty &= -\epsilon\cos\theta_\infty, \quad |v'|_\infty = \epsilon\sin\theta_\infty, \\ |p'|_\infty &= \epsilon\gamma M_\infty, \qquad |\rho'|_\infty = |p'|/\gamma; \end{aligned} \tag{9}$$

entropy waves $[\omega = k_\infty\cos\theta_\infty]$:

$$\begin{aligned} |u'|_\infty &= 0, \quad |v'|_\infty = 0, \\ |p'|_\infty &= 0, \quad |\rho'|_\infty = \epsilon M_\infty; \end{aligned} \tag{10}$$

vorticity waves $[\omega = k_\infty\cos\theta_\infty]$:

$$\begin{aligned} |u'|_\infty &= \epsilon\sin\theta_\infty, \quad |v'|_\infty = \epsilon\cos\theta_\infty, \\ |p'|_\infty &= 0, \qquad |\rho'|_\infty = 0, \end{aligned} \tag{11}$$

where ϵ is a small non-dimensional parameter representing the free-stream wave magnitude. The parameter k_∞ is the free-stream wavenumber vector with components k_x and k_y in the streamwise and wall-normal direction, respectively, i.e.

$$k_x = k_\infty\cos\theta_\infty, \qquad k_y = -k_\infty\sin\theta_\infty, \tag{12}$$

where θ_∞ is the incident wave angle in the free-stream relative to the streamwise direction as shown in figure 1.

The frequency of a disturbance wave is characterized by a dimensionless frequency F defined by

$$F = \frac{\omega^* \mu^*_\infty}{\rho^*_\infty u^{*2}_\infty}, \tag{13}$$

where ω^* is dimensional circular frequency. A non-dimensional circular frequency ω can also be defined as

$$\omega = \omega^* L^*/u^*_\infty. \tag{14}$$

Case	Frequency (F)	θ_∞	ϵ
F.1	2.2×10^{-4}	0°	5.0×10^{-4}
F.2	2.2×10^{-4}	15°	5.0×10^{-4}
F.3	1.6×10^{-4}	22.5°	5.0×10^{-4}
S.1	2.2×10^{-4}	0°	5.0×10^{-4}
S.2	2.2×10^{-4}	22.5°	5.0×10^{-4}
S.3	2.2×10^{-4}	45°	5.0×10^{-4}
S.4	2.2×10^{-4}	67.5°	5.0×10^{-4}
S.5	1.6×10^{-4}	0°	5.0×10^{-4}
S.6	1.6×10^{-4}	22.5°	5.0×10^{-4}
S.7	1.6×10^{-4}	45°	5.0×10^{-4}
S.8	1.6×10^{-4}	67.5°	5.0×10^{-4}
E.1	2.2×10^{-4}	0°	5.0×10^{-4}
E.2	2.2×10^{-4}	22.5°	1.0×10^{-5}
E.3	2.2×10^{-4}	45°	1.0×10^{-5}
E.4	2.2×10^{-4}	67.5°	1.0×10^{-5}
E.5	1.6×10^{-4}	0°	1.0×10^{-5}
E.6	1.6×10^{-4}	22.5°	1.0×10^{-5}
E.7	1.6×10^{-4}	45°	1.0×10^{-5}
E.8	1.6×10^{-4}	67.5°	1.0×10^{-5}
V.1	2.2×10^{-4}	0°	5.0×10^{-4}
V.2	2.2×10^{-4}	22.5°	1.0×10^{-5}
V.3	2.2×10^{-4}	45°	1.0×10^{-5}
V.4	2.2×10^{-4}	67.5°	1.0×10^{-5}
V.5	1.6×10^{-4}	0°	1.0×10^{-5}
V.6	1.6×10^{-4}	22.5°	1.0×10^{-5}
V.7	1.6×10^{-4}	45°	1.0×10^{-5}
V.8	1.6×10^{-4}	67.5°	1.0×10^{-5}

TABLE 1. Case F. Free-stream fast acoustic waves. Case S. Free-stream slow acoustic waves. Case E. Free-stream entropy waves. Case V. Free-stream vorticity waves.

The relation between the non-dimensional circular frequency ω and F is

$$F = \frac{\omega}{R}. \tag{15}$$

Because receptivity to fast acoustic waves has been discussed in our previous paper (Ma & Zhong 2003*b*), three groups of computational cases are studied in this paper for receptivity to free-stream slow acoustic waves, entropy waves and vorticity waves, respectively. For each group, eight different test cases with different combination of two different frequencies, i.e. $F = 1.6 \times 10^{-4}$, 2.2×10^{-4}, and four different incident wave angles, i.e. $\theta_\infty = 0°$, 22.5°, 45° and 67.5° are considered to study parametric effects of frequencies and disturbance incident angles. These two frequencies are chosen because the branch II neutral stability point of the second mode and the peak of mode II are located inside the computational domain. Both of them can move outside the computational domain for lower frequencies according to our previous results (Ma & Zhong 2003*a*). The flow conditions of the three groups of computational cases are given in table 1. Numerical results about these cases will be compared with our previous results shown in Ma & Zhong (2003*b*).

For each case of the boundary-layer response to a forcing wave, the unsteady computations are carried out for a number of periods in time until the numerical

solutions reach a periodic state. After that, unsteady computations are conducted for one additional period in time, so that a temporal Fourier analysis is performed on the results of the unsteady flow to obtain the amplitudes and phase angles of disturbances in the following form:

$$\phi'(x, y, t) = |\phi'(x, y)| \exp(\mathrm{i}[\psi'(x, y) - \omega t]), \tag{16}$$

where $|\phi'(x, y)|$ and $\psi'(x, y)$ are local amplitudes and phase angles of the induced waves in the flow field, respectively. From the wave amplitudes and phase angles, streamwise wavenumbers and growth rates of the disturbance waves can be extracted from the numerical solutions near the wall by

$$\alpha_r = \frac{\mathrm{d}|\psi'|}{\mathrm{d}x}, \tag{17}$$

$$\alpha_i = -\frac{1}{|\phi'|}\frac{\mathrm{d}|\phi'|}{\mathrm{d}x}. \tag{18}$$

The values calculated by using (17) and (18) correspond to the streamwise wavenumber and growth rate of a single wave if the numerical solutions are dominated by a single discrete wave mode in a local region. Then phase velocity of the single wave is given by

$$a = \omega/\alpha_r. \tag{19}$$

If the local numerical solutions contain a mixture of two or more wave modes, the values of α_r and α_i calculated by (17) and (18) do not represent wavenumber and growth rate of a single wave. Instead, they are the result of a modulation of these wave modes.

5. Oblique shock and free-stream disturbance interaction

The theoretical results of the interaction of linear free-stream disturbances with oblique shock waves (McKenzie & Westphal 1968) are compared with current numerical results in this section. These theoretical results can be used to validate the current numerical results on unsteady flows. The linear interaction theory also helps to analyse the receptivity mechanisms.

Figure 2 shows an oblique shock wave with a shock angle θ_{shk}, incident free-stream forcing waves with angle θ_∞ and wavenumber k_∞, transmitted acoustic waves with angle θ_2 and wave number k_2, and transmitted entropy/vorticity waves with angle θ_3 and wavenumber k_3. The angle is positive if its relative position to the x-axis is consistent with that shown in figure 2. Otherwise, the angle is negative. Figure 2 also depicts the normal and tangential components of the free-stream velocity and the vector of the incident wavenumber relative to the direction of shock. Given amplitude, incident wave angle of free-stream disturbances, and oblique shock angle (between 15.8° and 13.4° as shown in figure 4 of Ma & Zhong 2003*a*), the angle and amplitude of transmitted disturbances behind the shock can be calculated by using McKenzie & Westphal's theory with errata in Anyiwo & Bushnell (1982). The incident waves can be planar fast acoustic waves, slow acoustic waves, entropy waves, or vorticity waves.

For the case of incident fast acoustic waves, it was found that a good agreement is achieved between the theoretical prediction and the numerical simulation (Ma & Zhong 2003*b*). However, for incident free-stream slow acoustic waves, there is no theoretical prediction available because the shock angle is larger than the critical shock angle allowed in the linear analysis (McKenzie & Westphal 1968). From the

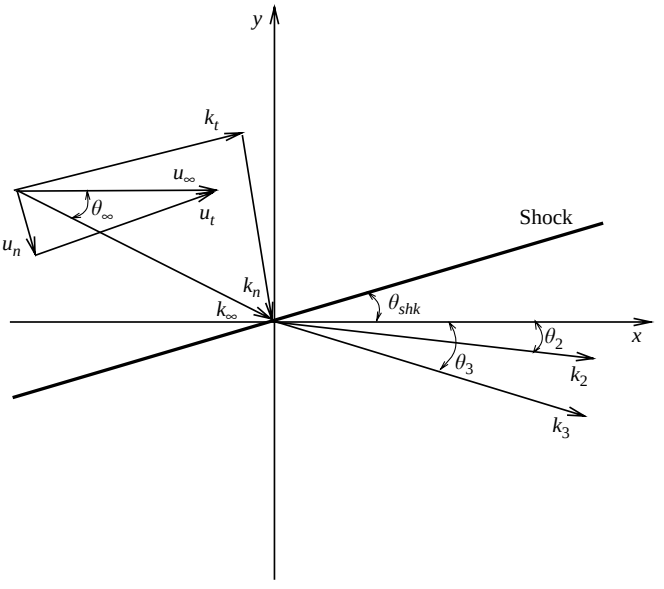

FIGURE 2. Configuration of the interaction between free-stream forcing disturbances and a planar oblique shock.

linear analysis, the wave angles of the generated acoustic waves behind the shock, θ_2, are the same for the cases of free-stream entropy waves and vorticity waves at the same incident wave angles. In addition, the wave angles of the generated acoustic waves behind the shock are independent of the frequencies of the incident waves in front of the shock. Therefore, incident entropy waves and vorticity waves are discussed together here.

Figure 3 shows the distribution of wave angles of the generated fast acoustic waves (θ_2) induced by free-stream entropy/vorticity waves. Different lines stand for different incident wave angles (θ_∞). Owing to the change of shock angle as x increases, θ_2 gradually decreases along the streamwise direction for different incident wave angles. Figure 3 also shows that θ_2 increases with increasing incident wave angle θ_∞. In addition, it is found that θ_2 may become negative when θ_∞ is less than 37.5°. When incident wave angle decreases further to 30°, the transmitted wave angle θ_2 even becomes less than $-\theta_{shk}$. Figure 2 shows that direction of k_2 points to the free-stream after θ_2 becomes less than $-\theta_{shk}$.

Figure 4 shows contours of instantaneous pressure perturbations after the flow field reaches a periodic state for cases E.7 and V.7. Only part of the flow field is shown for clarity. From (9) to (12), pressure perturbations are characteristic of acoustic waves outside the boundary layer. Figure 4 shows that acoustic waves are generated by the interaction between the free-stream entropy/vorticity waves and the oblique shock. The phase velocity of acoustic waves immediately behind the shock can be calculated from (19) and is shown in figure 5. The oscillations in figure 5 are caused by interaction between the oblique shock and the reflected waves from the plate surface. According to McKenzie & Westphal's theory, both fast and slow acoustic waves can be generated behind the shock. Based on the results of phase velocity shown in figure 5, the generated acoustic waves are fast acoustic waves only. As expected, the wave patterns for the acoustic waves generated behind the shock in the region after $x^* > 0.2$ m are very similar for the two cases. This similarity is because

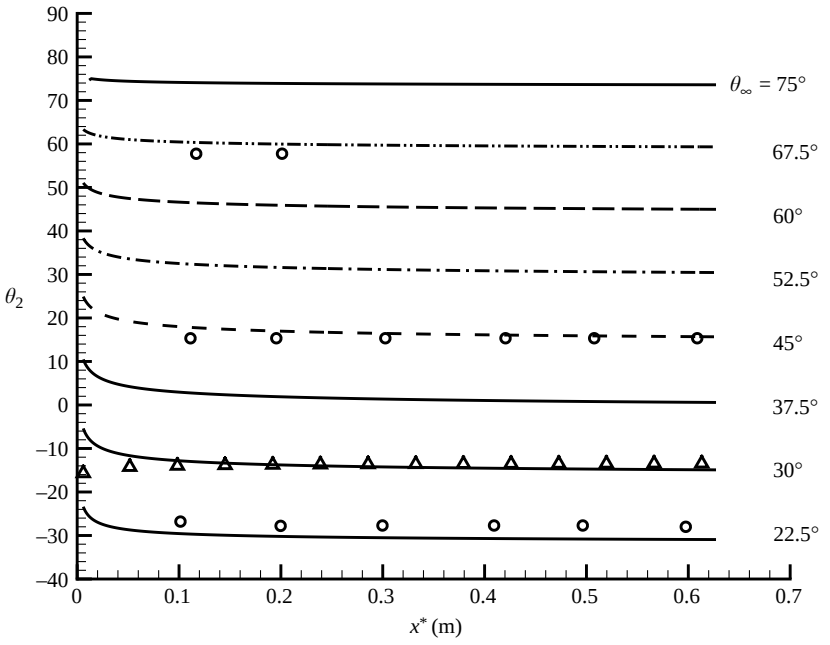

FIGURE 3. Wave angles of fast acoustic waves behind the shock generated by free-stream plane entropy/vorticity waves at different incident wave angles. Theoretical results are represented by different lines; ○, simulation results △, $-\theta_{shk}$ (shock angle) ($M_\infty = 4.5$, $F = 1.6 \times 10^{-4}$).

the acoustic waves generated behind the shock have the same wave angles for the two cases. In the region near the leading edge ($x^* < 0.2$ m), similarity is not clear, owing to significant changes of shock angle, and wave reflections from the wall. In the region away from the leading edge, the similar wave patterns consist of parallel contour lines in pressure perturbations behind the shock, which stands for the wave front of generated acoustic waves. A straight line is drawn along any one of the parallel lines, then the wave angle of generated acoustic waves is determined by the direction of wave propagation k_2 which is perpendicular to this straight line and points downstream because there are no waves propagating upstream for supersonic flow. The simulations shows that the wave angles of the generated acoustic waves (θ_2) are about 15.3° and the difference is less than 1.0° from $x^* = 0.15$ m to $x^* = 0.63$ m. The theoretically predicted wave angle of the generated acoustic waves (θ_2) is between 24.9° and 15.7° for $\theta_\infty = 45°$. The angle θ_2 decreases very fast (from 24.9° to 17.0°) in the region near the leading edge ($x^* < 0.15$ m) owing to a significant change of shock angle, while it is almost constant (between 17.0° and 15.7°) in the region between $0.15\,\text{m} < x^* < 0.63\,\text{m}$. Therefore, values of θ_2 measured from numerical simulations are very close to those from the linear interaction theory. This good agreement can confirm the accuracy of the current numerical simulation.

Similarly, figure 6 shows the contours of instantaneous pressure perturbations for cases E.8 and V.8. This figure shows wave patterns behind the shock that are more complex than those shown in figure 4. Figure 6 shows that there is a significant change in wave patterns in the region immediately behind the shock near the location $x^* = 0.21$ m. For $x^* < 0.21$ m, there are much clearer parallel wave patterns in the case of free-stream entropy waves than in the case of free-stream vorticity waves. The wave angles for parallel wave patterns shown in figure 6(*a*) behind the shock for

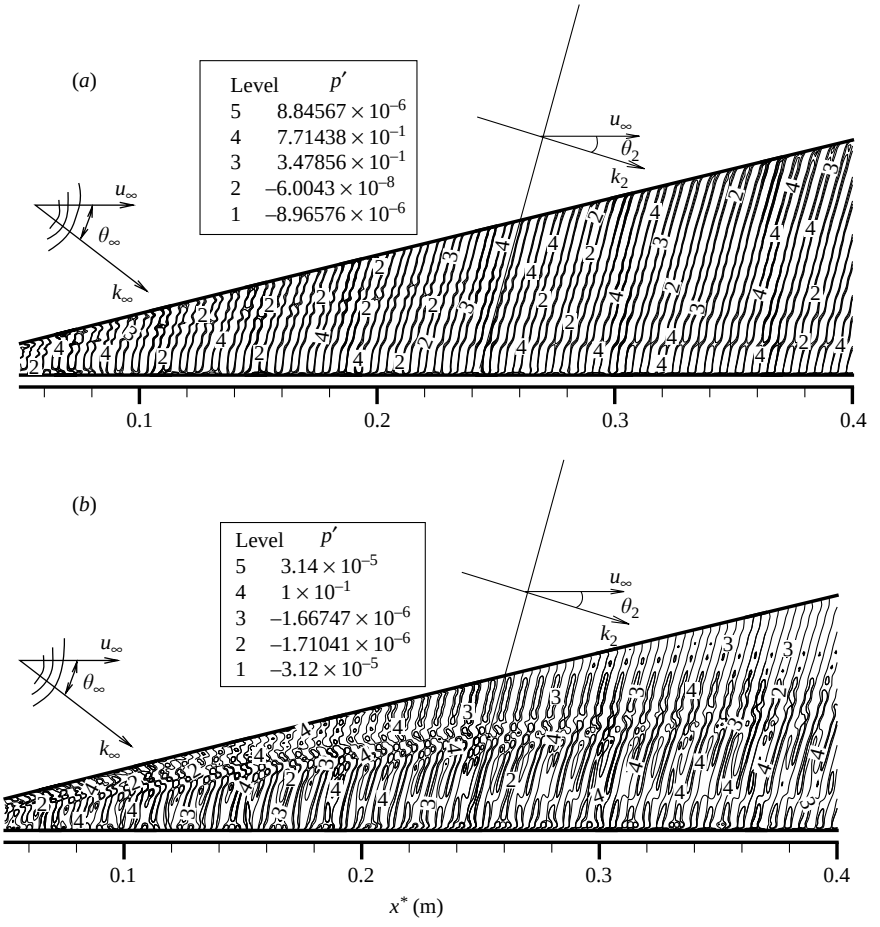

FIGURE 4. Fast acoustic waves (contours of instantaneous pressure perturbations) generated by (*a*) free-stream entropy waves (case E.7) and (*b*) free-stream vorticity waves (case V.7) ($M_\infty = 4.5$, $F = 1.6 \times 10^{-4}$ and $\theta_\infty = 45°$).

$x^* < 0.21$ m are between 62.0° and 57.7°. The theoretical calculations predict θ_2 to be in the range of 63.5° (at the inlet) to 58° (at the exit) as shown in figure 3. Values of θ_2 obtained from the theoretical prediction are in a very narrow range between 60.4° and 59.3° in the region of $0.1\,\text{m} < x^* < 0.63\,\text{m}$. Therefore, there is a very good agreement between the simulation and the theoretical prediction for $x^* < 0.21$ m. For $x^* > 0.21$ m, figure 6(*a*) shows that parallel wave patterns behind the shock disappear. Instead, new parallel wave patterns with wave angle close to −57.4° are generated between the shock layer and the boundary layer. These are caused by strong wave reflections from the wall after the impingement of the generated acoustic waves on the wall. As a result, the wave angles of reflected acoustic waves from the wall are almost equal to the wave angles of generated acoustic waves behind the shock and the signs of wave angles are opposite to each other. The wave angles after reflection are not exactly equal to the incident wave angles because of diffraction inside the boundary layer. The reflected acoustic waves propagate downstream and hit the oblique shock from behind. Because the flow is supersonic ahead of the shock, no disturbances are created ahead of the shock as a result of the impingement of reflected acoustic waves from behind the shock. However, the acoustic waves incident upon the shock from behind, which

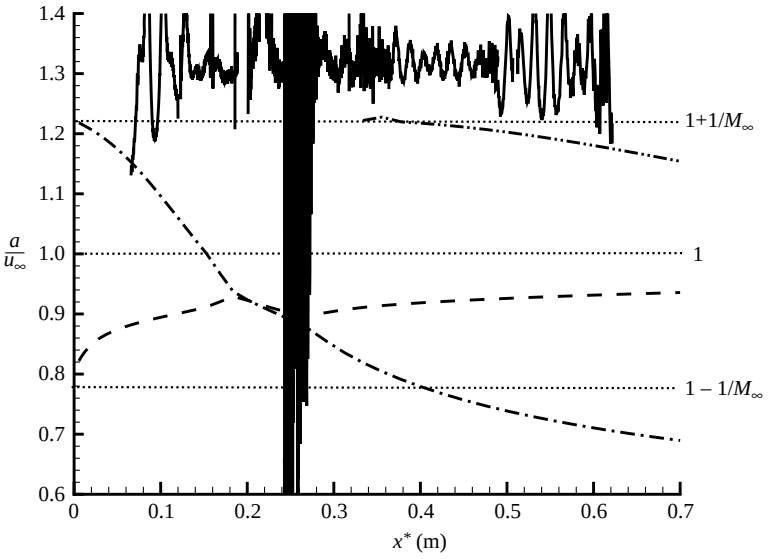

FIGURE 5. Distribution of phase velocities of disturbances immediately behind the shock for case E.7 ($M_\infty = 4.5$, $F = 1.6 \times 10^{-4}$ and $\theta_\infty = 45°$). - - -, LST (Mack modes); –·–, LST (mode I); –··–, LST (mode II); —, $J = 121$.

are reflected from the wall, create new components of acoustic waves, entropy waves and vorticity waves behind the shock. Therefore, the pressure perturbations shown in figure 6(*a*) are the result of multiple reflections between the shock and wall surface. Because of interaction between the acoustic waves generated and reflected behind the shock and the acoustic waves reflected from the wall, there are no clear parallel wave patterns shown behind the shock in the region of $x^* > 0.21$ m in figure 6(*a*). For acoustic waves generated by free-stream vorticity waves, shown in figure 6(*b*), the wave angle of the parallel wave patterns in the region $x^* < 0.21$ m is also close to 57.7°, which is in good agreement with theoretical prediction. However, there are much more complicated wave patterns resulting from the interaction between generated and reflected acoustic waves behind the shock and reflected acoustic waves from the wall as compared with that shown in figure 6(*a*).

As shown in figure 3, the wave angles of the generated acoustic waves behind the shock, θ_2, decrease when the incident wave angles θ_∞ decrease. For $\theta_\infty = 22.5°$, the theoretical values of θ_2 are between $-23.4°$ (at the inlet) and $-30.9°$ (at the exit). In particular, θ_2 is between $-29.6°$ and $-30.9°$ in the downstream region of $x^* > 0.1$ m. Therefore, the direction of wavenumber vector, k_2, points towards the free-stream because θ_2 is smaller than the shock angle, $-\theta_{shk}$. As shown in figure 4 of Ma & Zhong (2003*a*), the shock angle θ_{shk} is between 15.8° and 13.4°. Figure 7 shows contours of instantaneous pressure perturbations induced by (*a*) free-stream entropy waves (case E.6) and (*b*) free-stream vorticity waves (case V.6). Very similar wave patterns in the region immediately behind the shock are observed for the two cases. This figure shows that the direction of generated acoustic waves k_2 points to the free-stream direction, which is in agreement with the theoretical prediction. In addition, θ_2, which can be measured from wave fronts shown in figures 7(*a*) and 7(*b*), is between $-27.7°$ and $-26.8°$ in the region after $x^* > 0.1$ m. Again, the wave angles of the generated acoustic waves measured from the results of numerical simulations agree well with the theoretical results.

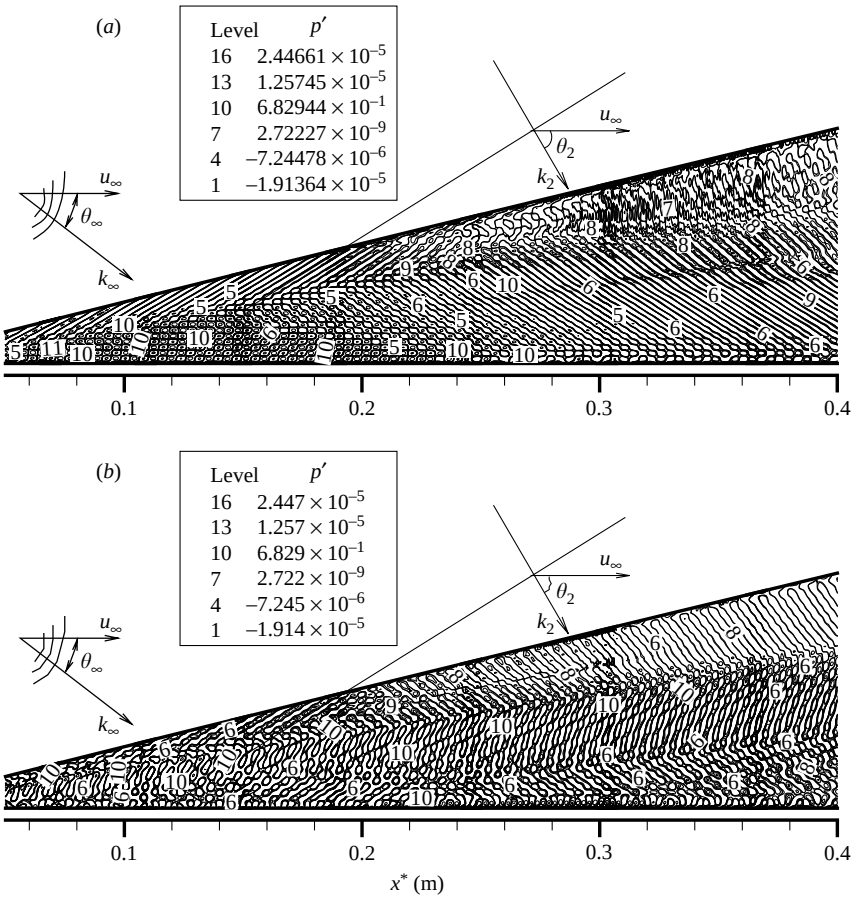

FIGURE 6. Fast acoustic waves (contours of instantaneous pressure perturbations) generated by (*a*) free-stream entropy waves (case E.8) and (*b*) free-stream vorticity waves (case V.8) ($M_\infty = 4.5$, $F = 1.6 \times 10^{-4}$ and $\theta_\infty = 67.5°$).

For the case of free-stream entropy/vorticity waves at $\theta_\infty = 0°$, there is no theoretical result on the wave angles of the acoustic waves generated behind the oblique shock, because θ_∞ is smaller than the critical incident wave angle (McKenzie & Westphal 1968). Though the wave angles of the generated acoustic waves cannot be predicted by linear interaction theory, they can be obtained by the numerical simulations of the Navier–Stokes equations. The instantaneous pressure perturbations induced by free-stream entropy waves and vorticity waves at the incident wave angle of $\theta_\infty = 0°$ (cases E.5 and V.5) are plotted in figure 8. Again, there are very similar wave patterns in instantaneous pressure perturbations between the two test cases. The wave angle θ_2 obtained from the numerical simulation is between $-47.5°$ and $-46.6°$ in the region of $x^* > 0.1$ m. The results for θ_2 are measured directly from wave fronts shown in figure 8. In addition, the wave angles measured from figure 8(*a*) for the case of free-stream entropy waves are the same as those measured at the same location in figure 8(*b*) for the case of free-stream vorticity waves.

Except for $\theta_\infty = 0°$, the results of θ_2 from the numerical simulations are also compared with the theoretical results in figure 3. Because θ_2 measured from the simulation results of pressure perturbations for the cases of free-stream entropy waves are the

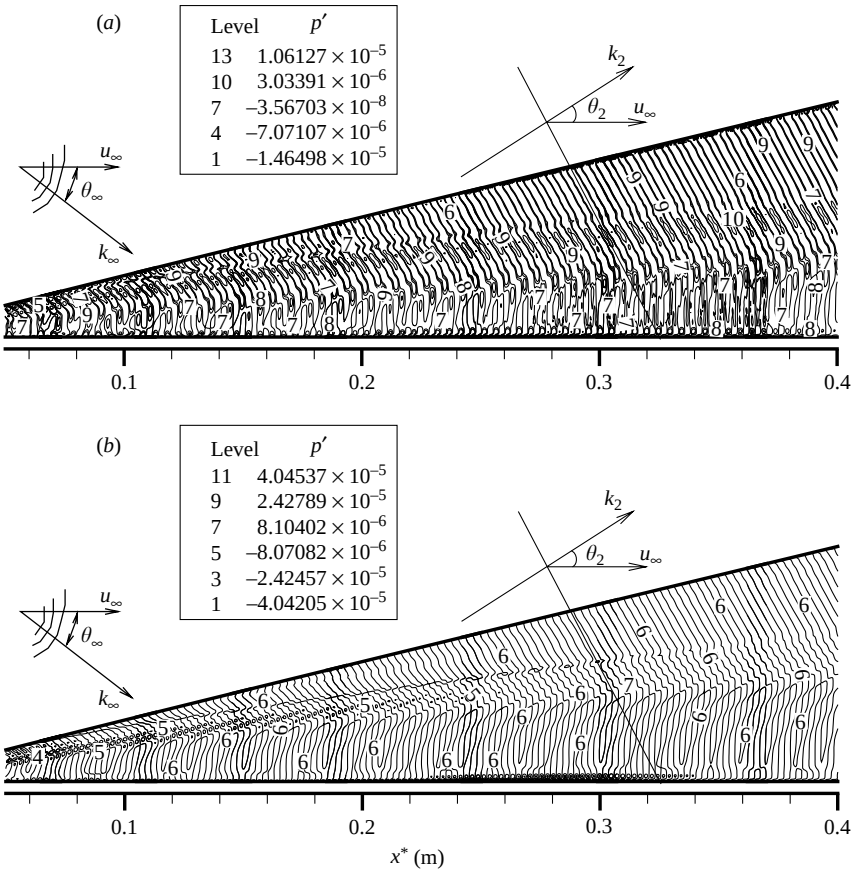

FIGURE 7. As for figure 6, but (*a*) case E.6, (*b*) case V.6 and $\theta_\infty = 22.5°$.

same as those generated by vorticity waves at the same incident wave angles and at the same location, only simulation results for the cases of free-stream entropy waves are plotted in figure 3 by symbol '○' for comparison. Overall, the figure shows that there is good agreement between the results obtained from the numerical simulations and those of the theoretical predications, which demonstrates that our numerical code based on shock-fitting methods can correctly simulate the interaction between free-stream disturbances and oblique shock. Furthermore, numerical results can consider wave reflections from wall surface and give more detail information about complex wave patterns.

Figure 9 compares amplitudes of pressure perturbations immediately behind the oblique shock for cases E.8 and V.8. For incident free-stream entropy waves (case E.8), there is good agreement between the numerical results and the theoretical predictions in the amplitudes of acoustic waves generated behind the shock, in the region downstream. However, because of strong wave reflections between the shock and the boundary layer near the leading edge, there are strong oscillations in the numerical results near the leading edge. Since such wave reflections are not considered in the linear theory, the theoretical prediction is not expected to agree with the simulation results in the leading-edge region. For the case of incident vorticity waves, there are visible differences between the numerical results and theoretical predictions in the

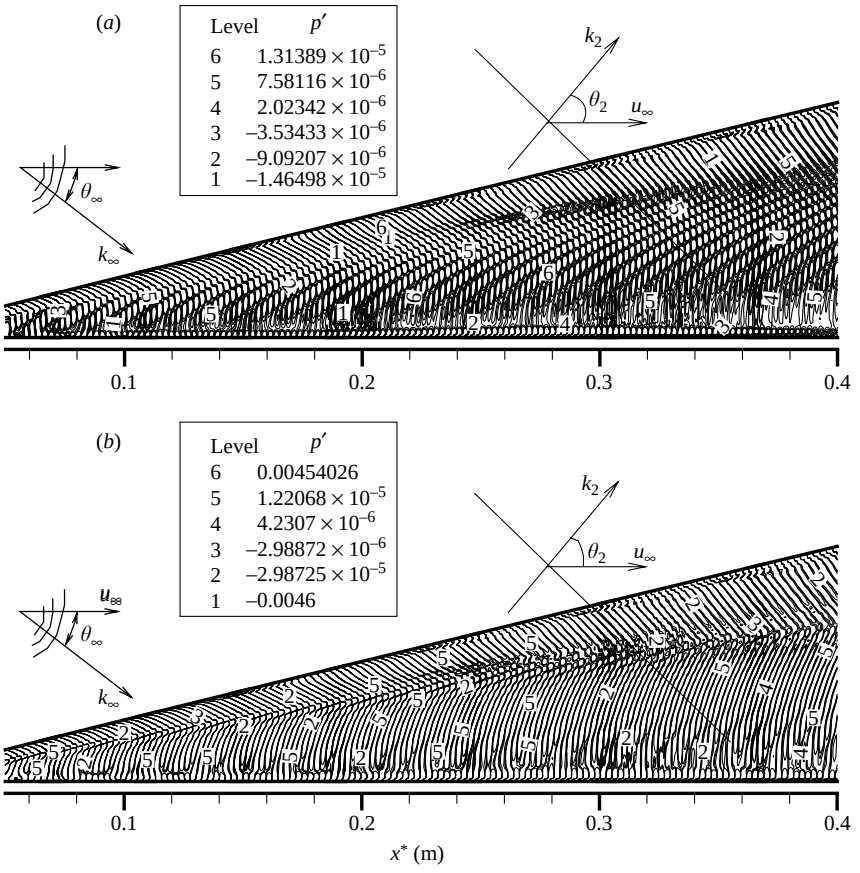

FIGURE 8. As for figure 6, but (*a*) case E.5, (*b*) case V.5 and $\theta_\infty = 0°$.

amplitude of acoustic waves generated behind the shock. These differences may be caused by stronger wave reflections between the shock and the boundary layer.

For cases E.7 and V.7, figure 9(*b*) shows that the theoretical amplitudes of the fast acoustic waves generated by free-stream vorticity waves are almost the same as those induced by free-stream entropy waves. The amplitudes of the fast acoustic waves generated by free-stream entropy waves and vorticity waves can be very different at other incident wave angles, although the same wave angles θ_2 are obtained for the two types of waves with the same incident angles. For example, at $\theta_\infty = 67.5°$, the amplitudes of the acoustic waves generated by free-stream entropy waves are stronger than those generated by free-stream vorticity waves (figure 9). However, the opposite is true for the cases of $\theta_\infty = 22.5°$ shown in figure 10. At $\theta_\infty = 22.5°$, the amplitude of the acoustic waves generated by free-stream entropy waves is weaker than that by free-stream vorticity waves. Figure 10 also shows that there are strong oscillations in the amplitudes of the pressure perturbations, which is a result of the interaction between the generated acoustic waves and the oblique shock. Therefore, figure 10 shows obvious and expected differences between the simulation results and theoretical predictions. At $\theta_\infty = 0°$, theoretical prediction is not available. Figure 10(*b*) compares only the simulation results for the amplitudes of the fast acoustic waves generated by free-stream entropy waves and those by free-stream vorticity waves for $\theta_\infty = 0°$. It shows that there are very similar shapes between the two cases, while the

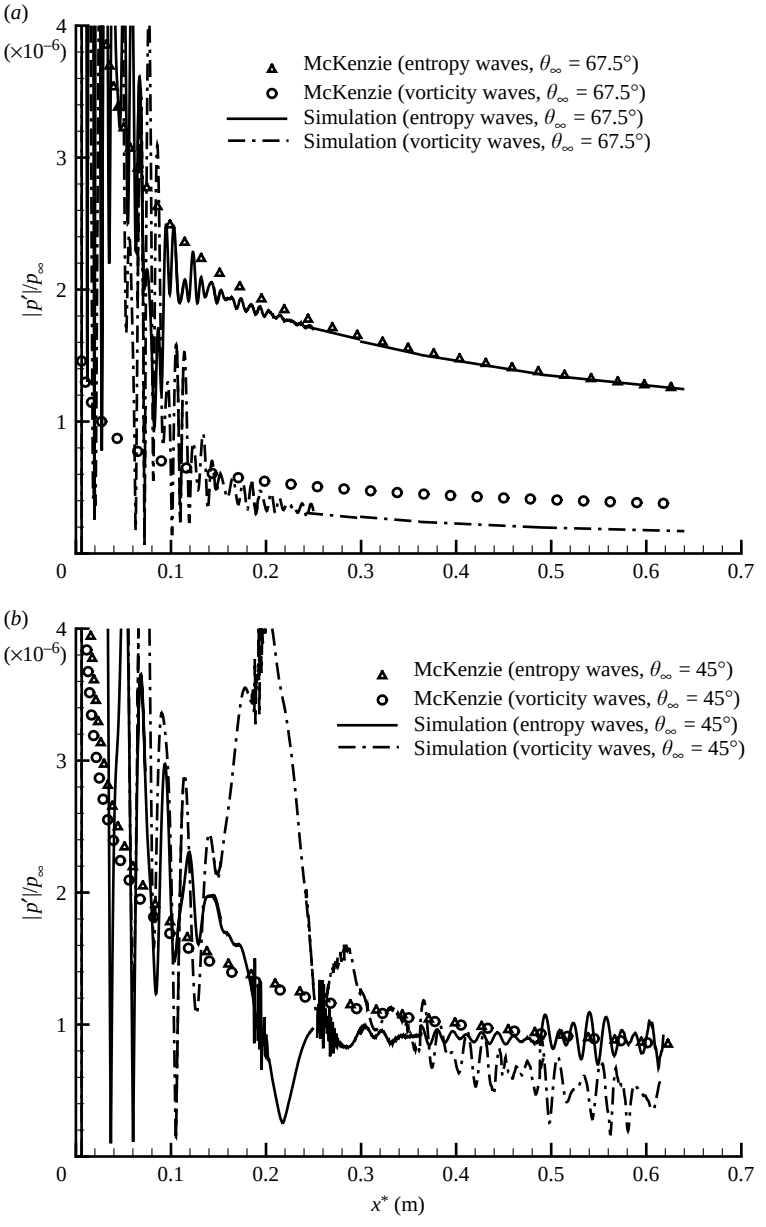

FIGURE 9. Comparison of the pressure perturbation amplitudes for fast acoustic waves immediately behind the shock generated by free-stream entropy waves (cases E.7 and E.8) and vorticity waves (cases V.7 and V.8) with different free-stream wave angles ($M_\infty = 4.5$ and $F = 1.6 \times 10^{-4}$).

amplitude of fast acoustic waves generated by free-stream vorticity waves are much stronger than those generated by free-stream entropy waves.

6. Receptivity to free-stream slow acoustic waves

This section considers planar free-stream slow acoustic waves with different frequencies and different incident wave angles (θ_∞), i.e. cases S.1 to S.8 will be discussed.

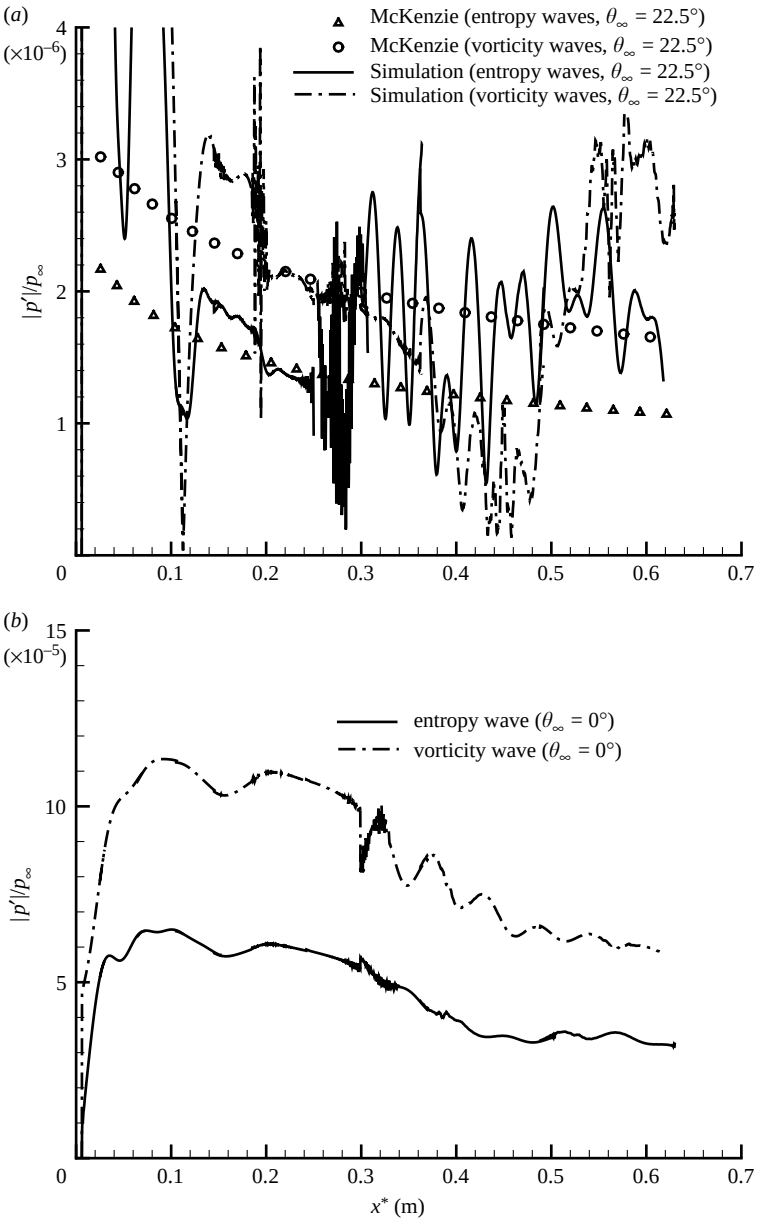

FIGURE 10. As for figure 9, but for cases E.5, E.6, V.5 and V.6.

6.1. *Free-stream slow acoustic waves with* $F = 2.2 \times 10^{-4}$ *and* $\theta_\infty = 0°$ (*case S.1*)

Figure 11 shows the contours of instantaneous density perturbations after the flow field reaches a periodic state in time. For clarity only a part of the flow field is shown in the figure. The position of the oscillating oblique shock is presented as the upper boundary of the flow field. Because the amplitude of the free-stream disturbances is small, the shock oscillations are not visible. Behind the shock, there are strong transmitted acoustic waves propagating in the direction almost parallel to the wall. The dimensionless phase velocity is about $1 - 1/M_\infty$, which indicates that

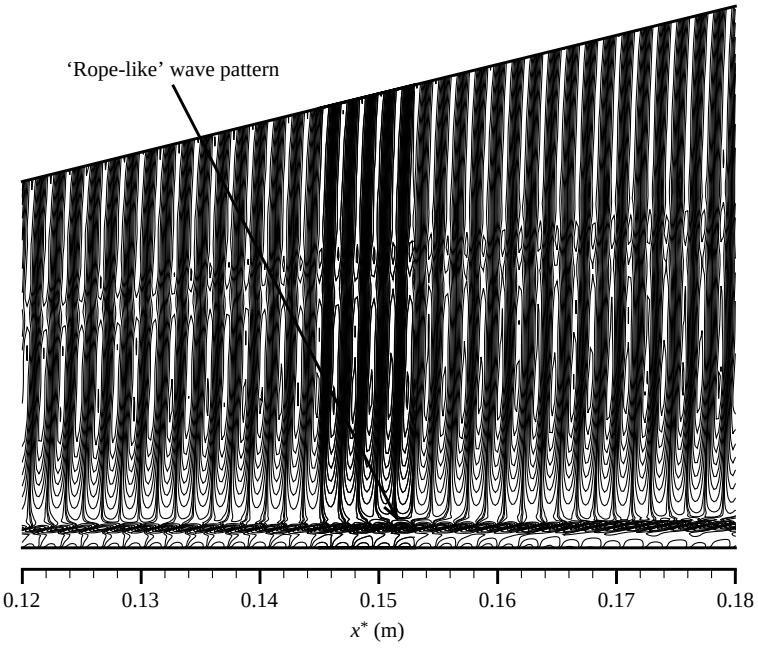

FIGURE 11. Contours of density perturbations due to free-stream plane slow acoustic waves (case S.1) ($M_\infty = 4.5$, $F = 2.2 \times 10^{-4}$ and $\theta_\infty = 0°$).

the transmitted waves are slow acoustic waves. From the results of the base flow shown in Ma & Zhong (2003*a*), the displacement thickness of the boundary layer is about $y/L = 12.9$. In figure 11, there is a rope-like wave pattern near the edge of the boundary layer for $0.1\,\mathrm{m} < x^* < 0.2\,\mathrm{m}$, which is the typical signature of the second-mode Mack waves.

Figure 12 compares the amplitudes of pressure disturbances along different streamwise grid lines for free-stream slow acoustic waves and free-stream fast acoustic waves. $J = 1$ stands for the grid line near the wall surface, while $J = 121$ represents the grid line immediately behind the shock. The dimensionless amplitude of the free-stream acoustic waves is also plotted as a dotted line. Because of the interaction between the shock and the free-stream forcing waves, there is a jump in the amplitudes of pressure perturbations across the shock for both cases. The amplitudes of pressure perturbations behind the shock are larger for the free-stream slow acoustic waves than for the free-stream fast acoustic waves. After passing the shock, the transmitted acoustic waves propagate downstream, penetrate the boundary layer, impinge and reflect from the wall. The interaction between forcing waves and viscous boundary-layer flow leads to the generation of boundary-layer disturbance waves. As discussed in Ma & Zhong (2003*b*), the dominant boundary-layer disturbances in receptivity to free-stream fast acoustic waves are mode I waves, which are always stable and convert to the second-mode waves. Figure 12 shows that the development of pressure perturbations on the wall induced by free-stream slow acoustic waves has a totally different characteristic from that induced by free-stream fast acoustic waves. Free-stream slow acoustic waves do not generate mode II waves in the region around $x^* = 0.3\,\mathrm{m}$. Instead, the Mack modes are generated upstream with a peak located around $x^* = 0.14\,\mathrm{m}$. The dominant boundary-layer waves generated by slow acoustic waves are recognized to be the second-mode waves from the 'rope-like' wave pattern

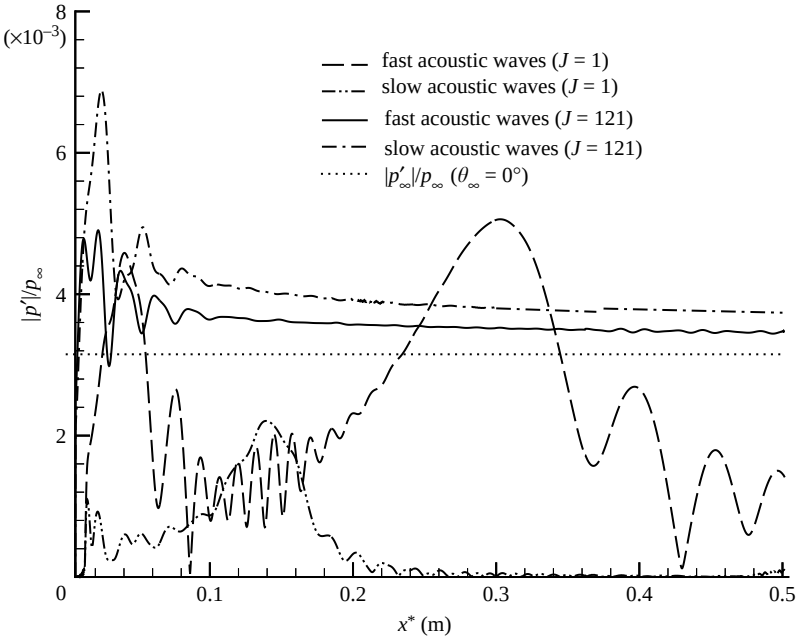

FIGURE 12. Distributions of pressure perturbation amplitudes induced by free-stream plane slow acoustic waves (case S.1). The results are compared with the corresponding results induced by free-stream fast acoustic waves (case F.1) ($M_\infty = 4.5$, $F = 2.2 \times 10^{-4}$ and $\theta_\infty = 0°$).

(Pruett & Zang 1995) shown in figure 11, which can also be confirmed by comparing local wave structures with eigenfunctions of the second mode from the LST calculations. Figure 13 shows the comparison of the fluctuation profiles at $x^* = 0.14$ m. There is a very good agreement between the results from the LST and DNS for profiles inside the boundary layer ($y/L < 12.9$). The strong fluctuation in temperature profile near the edge of the boundary layer is also characteristic of the second mode.

The difference in the receptivity to free-stream fast and slow acoustic waves can be explained from the LST results for the phase velocities of boundary-layer normal modes. Figure 14 compares the phase velocities of boundary-layer disturbances induced by free-stream planar slow acoustic waves with those induced by free-stream fast acoustic waves. The receptivity process in the case of free-stream fast acoustic waves is the excitation of stable mode I near the leading edge, followed by the excitation of the second Mack mode by mode I downstream. Still further downstream, a strong mode II, which is always stable, is generated by direct interaction with the fast acoustic waves. Figure 14 shows that this receptivity mechanism is essentially different from that of free-stream slow acoustic waves. For receptivity to slow acoustic waves, figure 14 shows that the phase velocities of the induced boundary-layer disturbances are very close to that of the first mode obtained from the LST results, which indicates that the first Mack modes are generated by the forcing free-stream slow acoustic waves. This numerical result is consistent with Fedorov & Khokhlov's (2001) theoretical prediction. After passing the synchronization point ($x^* = 0.11$ m) between mode I and the first mode, the first-mode waves become the second Mack mode waves. The second-mode waves are significantly amplified and become dominant after entering the second-mode unstable region. The second-mode waves generated by the free-stream slow acoustic waves reach a peak amplitude of $|p'|/p_\infty = 0.002205$,

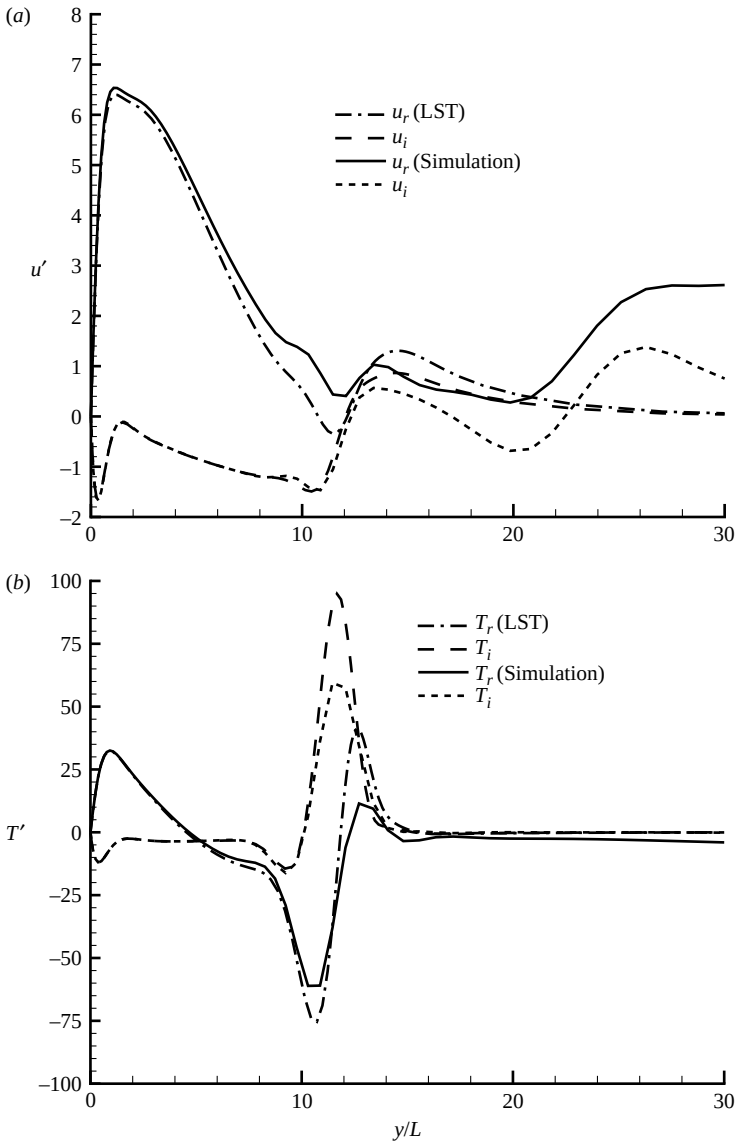

FIGURE 13. Comparison of wave structure of case S.1 with that of the second mode obtained by the LST ($M_\infty = 4.5$, $F = 2.2 \times 10^{-4}$, $\theta_\infty = 0^\circ$ and $Re_x = 1.0 \times 10^6$).

at the branch II neutral point located at $x^* = 0.14\,\mathrm{m}$ ($R = 1004$ and $RF = 0.221$). According to the LST results, the branch II neutral point of the second Mack mode is located at $R = 999.6$, which is in good agreement. After passing the branch II neutral point, the second-mode waves decay rapidly and lose dominance. As a result of modulation between different waves, there are strong oscillations in phase velocity curve for $x^* > 0.2\,\mathrm{m}$ (figure 14). The phase velocity curve is cut at $x^* = 0.24\,\mathrm{m}$ because boundary-layer disturbances induced by free-stream slow acoustic waves become very weak after this location.

From figure 12, the maximum amplitude of the second Mack mode waves at the branch II neutral stability point for the case of free-stream slow acoustic waves is

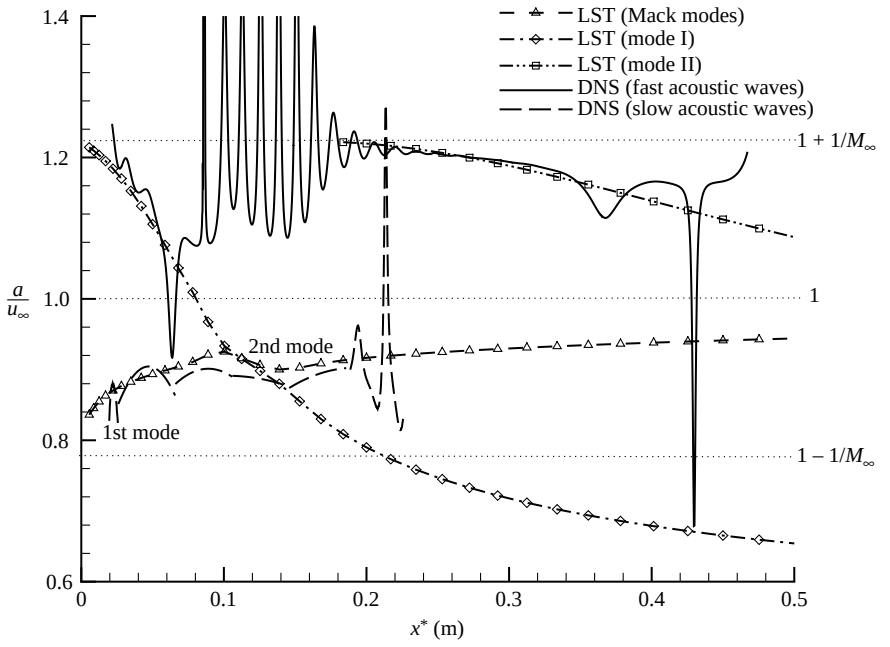

FIGURE 14. Distributions of phase velocities of boundary-layer disturbances induced by free-stream planar slow acoustic waves (case S.1) and comparison with those due to fast acoustic waves (case F.1) ($M_\infty = 4.5$, $F = 2.2 \times 10^{-4}$ and $\theta_\infty = 0^\circ$).

larger than that for the case of free-stream fast acoustic waves, which is qualitatively consistent with Fedorov & Khokhlov's (2002) theoretical results. In fact, there are strong oscillations in boundary-layer disturbances generated by free-stream fast acoustic waves due to a modulation between the second-mode waves and other waves. The actual component of the second-mode waves is even weaker than that shown in figure 12 in the region where the second-mode waves are expected to be dominant ($0.1\,\mathrm{m} < x^* < 0.2\,\mathrm{m}$). The component of the second-mode waves can be extracted from the overall disturbance field in the boundary layer by means of a spatial Fourier analysis, which was described in detail in Ma & Zhong (2003*b*) and is not repeated here. Quantitatively, the response coefficient of the second Mack mode, which is defined in Ma & Zhong (2003*b*) as the ratio of the maximum amplitude of induced boundary-layer disturbances to that of the forcing free-stream disturbance waves, is 0.7 for slow acoustic waves, as compared to 0.187 for fast acoustic waves after a decomposition of the second mode from total boundary-layer disturbances. Therefore, the receptivity of the second Mack mode to free-stream slow acoustic waves is about 3.7 times as large as that to free-stream fast acoustic waves for the current case of zero degree free-stream incident wave angle.

There are two reasons for the larger response coefficient of the second mode in the case of free-stream slow acoustic waves. First, the amplitudes of the transmitted slow acoustic waves are stronger than those of transmitted fast acoustic waves as shown in figure 12. Secondly, as shown in figure 14, the receptivity mechanisms of the boundary-layer second-mode waves to free-stream fast acoustic waves are different from those to free-stream slow acoustic waves. Specifically, in the case of free-stream fast acoustic waves, the second-mode (Mack modes) waves are induced through stable mode I waves which can have direct resonant interactions with the fast acoustic waves.

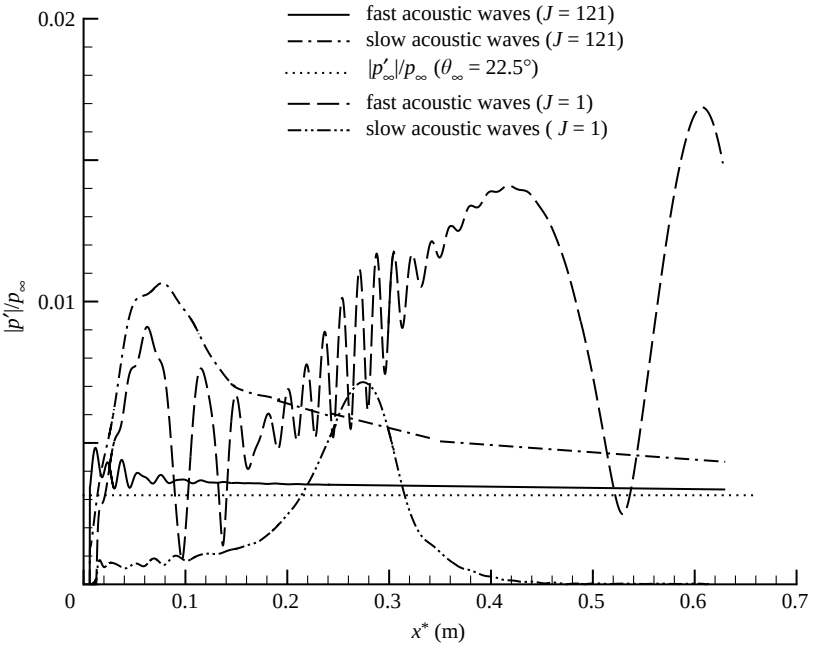

FIGURE 15. Distributions of pressure perturbation amplitudes induced by free-stream plane slow acoustic waves (case S.6). The results are compared with the corresponding results induced by free-stream fast acoustic waves (case F.3) ($M_\infty = 4.5$, $F = 1.6 \times 10^{-4}$ and $\theta_\infty = 22.5°$).

On the other hand, in the case of free-stream slow acoustic waves, the first mode (Mack modes) waves are generated directly from slow acoustic waves, then the first mode evolves to the second mode during propagation downstream. Since mode I is inherently much more stable than the first mode according to the LST analysis, the second Mack mode waves generated by the slow acoustic waves are much stronger. Because of these two reasons, the initial amplitudes of the second-mode waves are much stronger in receptivity to free-stream slow acoustic waves as compared to the receptivity to free-stream fast acoustic waves.

6.2. *Free-stream slow acoustic waves with* $F = 1.6 \times 10^{-4}$ *and* $\theta_\infty = 22.5°$ (*case S.6*)

Figure 15 compares the amplitudes of pressure perturbations immediately behind the shock ($J = 121$) and along the wall surface ($J = 1$) for receptivity to free-stream fast acoustic waves and slow acoustic waves. While the pressure perturbations behind the shock are slightly amplified and close to the amplitude of free-stream disturbances for the case of free-stream fast acoustic waves, there is a significant increase in the amplitudes of pressure perturbations across the shock for the case of free-stream slow acoustic waves. This is especially true near the leading edge. Again, boundary-layer disturbances are generated by the interaction between the transmitted acoustic waves and the viscous boundary-layer flow. Figure 15 shows that there are strong oscillations in the amplitudes of the pressure perturbations on the wall induced by free-stream fast acoustic waves. On the contrary, there is a smooth development for the pressure perturbations on the wall surface induced by free-stream slow acoustic waves. For the case of receptivity to free-stream slow acoustic waves, there is a smooth growth and decay of boundary-layer disturbances in the region $0.19\,\mathrm{m} < x^* < 0.38\,\mathrm{m}$. The dominant boundary-layer disturbances are identified to be the second mode by

comparing phase velocities and fluctuation profiles with the LST results. while, for the case of free-stream fast acoustic waves, a modulation of the second-mode with other waves is observed in the same region, and the receptivity of mode II waves is dominant.

As shown in figure 15, the maximum amplitude of the surface pressure perturbations due to forcing slow acoustic waves is located at $x^* = 0.274\,\mathrm{m}$ ($RF = 0.225$) with $|p'|/p_\infty = 0.00715$. The maximum amplitude occurs at the second-mode branch II neutral point. The maximum amplitude is about 3.24 times larger than in the case S.1 ($F = 2.2 \times 10^{-4}$). The physical mechanism for the effect from frequency on the peak value of the second mode will be explained at the end of § 6. The branch II location is predicted by LST to be located at $x^* = 0.2738\,\mathrm{m}$ ($RF = 0.2246$). Again, there is an excellent agreement between the value obtained by the numerical simulations and that predicted by LST. In addition, the branch II neutral stability point in term of RF (0.2246) for $F = 1.6 \times 10^{-4}$ is very close to the value of $RF = 0.2209$ in the previous case with $F = 2.2 \times 10^{-4}$, which is consistent with the results presented in Part 1 (Ma & Zhong 2003*a*) about locations of branch II neutral points for different frequencies.

Figure 15 shows that the amplitudes of the pressure perturbations at the second-mode branch II neutral point induced by forcing slow acoustic waves are weaker than those induced by forcing fast acoustic waves. This is different from the $F = 2.2 \times 10^{-4}$, $\theta_\infty = 0^\circ$ case. where the pressure perturbation amplitude at the second-mode branch II neutral point due to slow acoustic waves is stronger than that of the corresponding case of free-stream fast acoustic waves. However, the pressure perturbations of the case of free-stream fast acoustic waves near branch II neutral point are a result of the mixture of a number of wave modes, including the second Mack mode. There are multiple components of different waves, including the second mode waves, in boundary-layer disturbances induced by fast acoustic waves, which results in strong oscillations in amplitude distribution of pressure perturbations near the second-mode branch II neutral point. A wave mode decomposition is necessary in order to extract the component of the second mode in the results. After a decomposition of different components in boundary-layer disturbances, the component of the second mode waves induced by free-stream fast acoustic waves at the second-mode branch II neutral point is weaker than that by slow acoustic waves at the same location. Quantitatively, the response coefficients of the second Mack mode defined in Ma & Zhong (2003*b*) are 2.27 for the case of free-stream slow acoustic waves and 0.87 for the case of free-stream fast acoustic waves. Again, as explained in the previous case, the second-mode receptivity to free-stream slow acoustic waves is much stronger than that to free-stream fast acoustic waves.

Figure 16 compares the phase velocity distributions of boundary-layer disturbances with the corresponding LST results. Again, the phase velocity curve for the case of slow acoustic waves is cut at $x^* = 0.45$, where the induced boundary-layer disturbances almost die out as shown in figure 15. It shows that there is very good agreement in the phase velocities of boundary-layer disturbances induced by slow acoustic waves and that of Mack modes from the LST results, which confirms that Mack mode waves are directly generated near the leading edge by slow acoustic waves. The dramatic change in phase velocity of boundary-layer disturbances induced by fast acoustic waves shows that there are boundary-layer mode changes. This has been analysed in detail in Ma & Zhong (2003*b*).

Because the dominant Mack mode waves are generated directly by free-stream slow acoustic waves, the growth rate of the induced Mack mode waves can be compared with the second mode growth rates predicted by LST calculations. Figure 17 shows

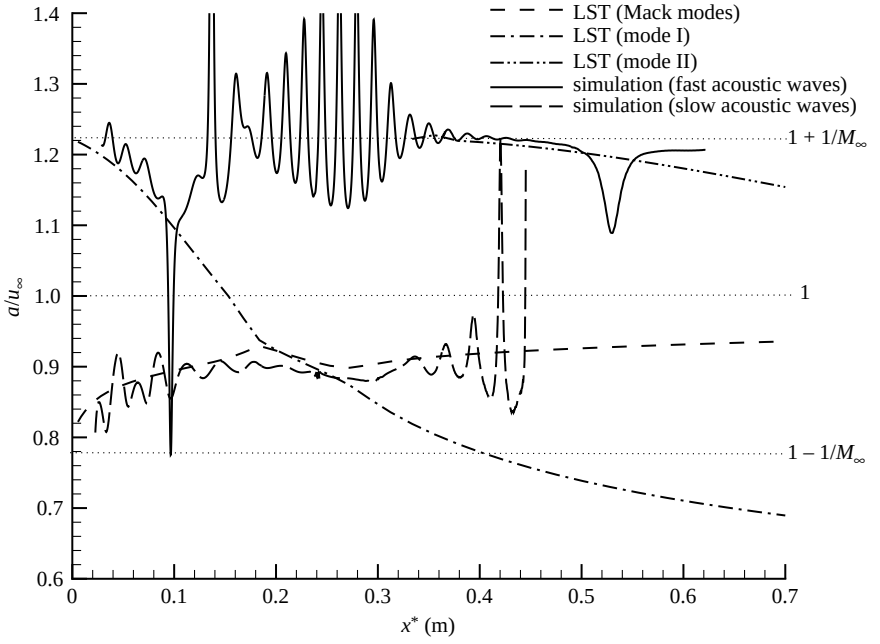

FIGURE 16. Distribution of phase velocities of boundary-layer disturbances due to free-stream plane slow acoustic waves (case S.6) and comparison with that due to fast acoustic waves (case F.3) ($M_\infty = 4.5$, $F = 1.6 \times 10^{-4}$ and $\theta_\infty = 22.5°$).

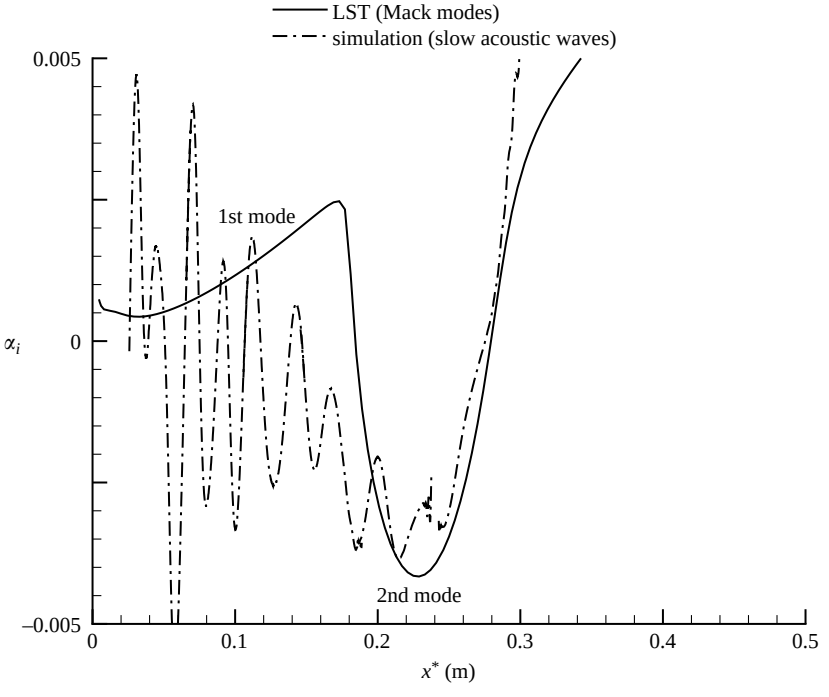

FIGURE 17. Comparison of growth rates of boundary-layer disturbances induced by free-stream slow acoustic waves (case S.6) obtained from DNS with the growth rates of Mack modes predicted by LST ($M_\infty = 4.5$, $F = 1.6 \times 10^{-4}$ and $\theta_\infty = 22.5°$).

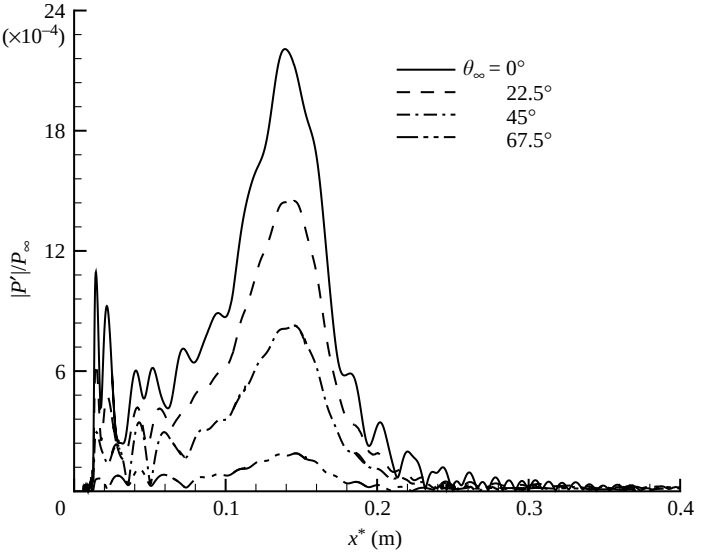

FIGURE 18. Distributions of pressure perturbations on the wall due to free-stream plane slow acoustic waves for cases S.1 to S.4 ($M_\infty = 4.5$, $F = 2.2 \times 10^{-4}$).

the comparison of growth rates. Overall, there is good agreement in the growth rates in the second-mode dominant region ($0.19\,\mathrm{m} < x^* < 0.38\,\mathrm{m}$) between the simulation results and the LST results, considering that there is a modulation between Mack mode waves and other waves induced by free-stream slow acoustic waves. Before the second Mack mode becomes dominant, the first mode waves are strongly modulated by other wave components, which leads to strong oscillations in the growth rate curve of the simulation results in the region with $x^* < 0.19\,\mathrm{m}$.

6.3. *Effect of frequencies and incident wave angles of forcing slow acoustic waves*

Figures 18 and 19 show the amplitudes of pressure disturbances on the wall for cases S.1 to S.8. Dominant second Mack mode waves are induced in all eight cases. For forcing waves of the same frequency but different incident wave angles, the induced second Mack mode waves reach their maximum perturbation amplitudes at the same branch II neutral stability location. With increasing incident wave angles, the peak amplitude of induced second Mack-mode waves decrease dramatically. In the receptivity process, boundary-layer disturbances are generated and amplified by transmitted slow acoustic waves due to resonant interactions between them. The resonant interaction happens only when the phase velocity of boundary-layer disturbances is close to that of forcing waves. For small incident angles, there are much stronger resonant interactions, because phase velocity of the first mode is closer to that of slow acoustic waves with zero incident angle. When incident angles increase, more perturbation energy from transmitted slow acoustic waves is reflected on the wall surface and carried by reflected acoustic waves. Accordingly, there is less perturbation energy transferred to boundary-layer disturbances. Therefore, the initial amplitude of the second-mode waves generated by slow acoustic waves is smaller for larger incident angles, which leads to smaller peak value at the branch II neutral point.

To quantitatively study the acoustic receptivity of the second mode, the receptivity can be measured by a branch I receptivity coefficient (Saric *et al.* 2002) defined as the ratio of the induced second-mode amplitude at the branch I neutral stability

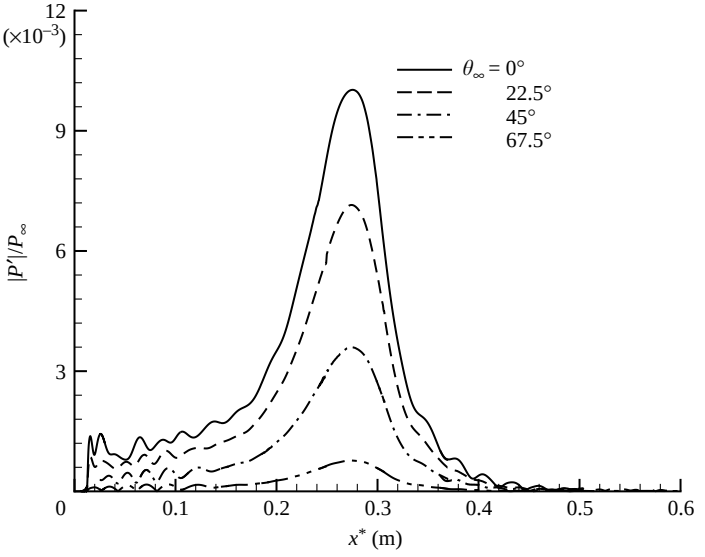

FIGURE 19. Distributions of pressure perturbations on the wall due to free-stream plane slow acoustic waves for cases S.5 to S.8 ($M_\infty = 4.5$, $F = 1.6 \times 10^{-4}$).

location to the amplitude of free-stream disturbances. From figure 17 (case S.6), the second-mode branch I neutral point, which is located at $x^* = 0.184$ m from the LST results, is difficult to determine from the simulation results. Since the growth of the second mode from the branch I to the branch II locations is mainly caused by the eigenmode growth of the unstable second mode, the second-mode amplitude at the branch I location can be determined by using the maximum wave amplitude at the branch II location and an integration of the spatial growth rates between the branch I and branch II locations (Ma & Zhong 2003*b*). Based on the LST results, the ratios between the amplitude of the second mode at the branch II and branch I locations are 5.2 and 10.6 for $F = 2.2 \times 10^{-4}$ and 1.6×10^{-4}, respectively. Figure 20 shows the receptivity coefficients of the second mode to free-stream acoustic waves as functions of the incident wave angles. For two different frequencies, the receptivity coefficients of the second mode to free-stream slow acoustic waves decrease dramatically with increasing incident wave angles. For comparison with receptivity to free-stream fast acoustic waves, the receptivity coefficients of the second mode to fast acoustic waves at $F = 2.2 \times 10^{-4}$ with different incident wave angles are also plotted in figure 20. It shows that, unlike the current cases of free-stream slow acoustic waves, the second-mode receptivity to free-stream fast acoustic waves is not very sensitive to the change of incident wave angles, which has been discussed in Ma & Zhong (2003*b*).

For the case of $\theta_\infty = 0°$, figure 20 shows that the receptivity coefficient of case S.5 ($F = 1.6 \times 10^{-4}$) is about 1.8 times larger than that of case S.1 ($F = 2.2 \times 10^{-4}$). As discussed before, there is a strong interaction between boundary-layer disturbances and transmitted slow acoustic waves. As a result, the induced boundary-layer disturbances, which are dominated by the Mack mode, keep growing before reaching the branch I neutral point, although the growth rate is relatively small compared with that of the unstable second mode. The second-mode branch I neutral point ($x^* = 0.184$ m) for $F = 1.6 \times 10^{-4}$ is located downstream of that for $F = 2.2 \times 10^{-4}$ ($x^* = 0.097$ m). Therefore, there is a much longer interaction range in terms of x^* for lower frequency, which leads to a larger initial amplitude of the second mode. This

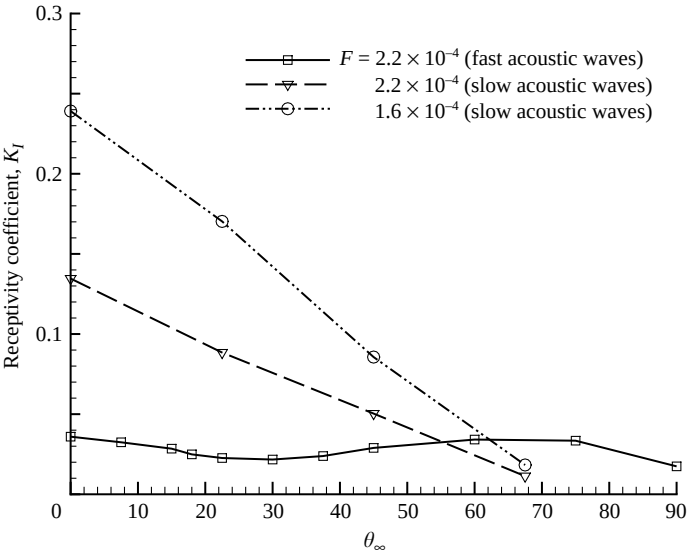

FIGURE 20. Receptivity coefficients of the second mode to free-stream acoustic waves *vs.* incident wave angles ($M_\infty = 4.5$).

is why receptivity coefficients in figure 20 are larger for lower frequency for the same incident wave angles. In addition, the integral of growth rate between the branch II and branch I neutral points are 5.2 and 10.6 for $F = 2.2 \times 10^{-4}$ and 1.6×10^{-4}, respectively. Thus, the second mode is much more amplified for lower frequency. For these two reasons, the second-mode peak values for case S.6 is about 3.24 times larger than that for case S.1.

7. Receptivity to planar free-stream entropy waves

Entropy waves in the free stream are characterized by fluctuations of temperature and density. In this section, supersonic boundary-layer receptivity to planar free-stream entropy waves (cases E.1 to E.8) are studied. The receptivity mechanisms of boundary-layer normal modes to free-stream entropy waves and the effect of incident wave angles on the receptivity are analysed by comparing the simulation results with those of LST calculations.

7.1. *Free-stream entropy waves at frequency* $F = 2.2 \times 10^{-4}$ (*case E.3*)

Figure 21 presents the contours of instantaneous entropy perturbations (*a*) and density perturbations (*b*) for case E.3. It shows that there are strong transmitted entropy waves behind the shock. The wave angles of the transmitted entropy waves in the current case, which can be measured from the contour lines of figure 21, are between 48.8° near the leading edge and 45.2° downstream. The theoretical values of the wave angles of transmitted entropy waves in the current case are between 52.0° and 46.8°, which are very close to simulation results. The difference is due to reflected waves from the wall surface and oscillation of oblique shock. The main focus of the present receptivity study is the generation of boundary-layer second mode waves by the receptivity process. From our previous study (Ma & Zhong 2003*a*), the second-mode waves are expected to be dominant in the region of $0.1\,\mathrm{m} < x^* < 0.2\,\mathrm{m}$. However, figure 21 shows that there is no clear rope-like second-mode wave structure near the edge of boundary layer in this region. The dominant component of the boundary-layer

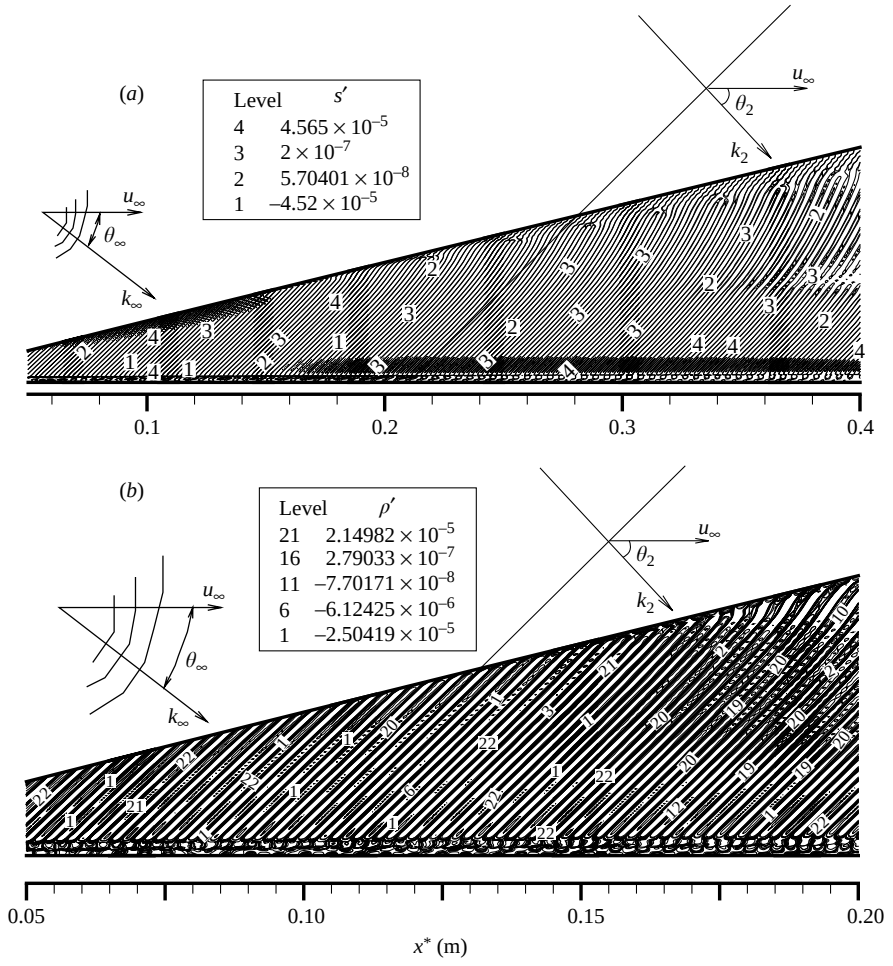

FIGURE 21. Contours of instantaneous entropy perturbations (*a*) and density perturbations (*b*) generated by free-stream entropy waves for case E.3 ($M_\infty = 4.5$, $F = 2.2 \times 10^{-4}$ and $\theta_\infty = 45°$).

disturbances induced by free-stream entropy waves can be identified by comparing the current results with LST and the receptivity results to fast acoustic waves.

The induced boundary-layer disturbances described by pressure perturbations on the wall surface are shown in figure 22. The amplitudes of pressure perturbations for case F.2 are also plotted in this figure for comparison. The wave angles for the transmitted fast acoustic waves behind the shock are approximately the same for these two cases although incident free-stream wave angles are different. Based on the discussion in § 5, fast acoustic waves are generated behind the shock by free-stream entropy waves. Here, the wave angle of generated acoustic waves is predicted by theoretical analysis to be between 17.0° and 15.7° in the region of $0.15\,\mathrm{m} < x^* < 0.63\,\mathrm{m}$. For case F.2, the wave angles of the transmitted fast acoustic waves are predicted to be between 18.4° and 15.2°. Therefore, the wave angles for fast acoustic waves behind the shock for the two cases compared in figure 22 are very close. However, the amplitude of transmitted acoustic waves in case F.2 is much larger than that of the current case. Hence, the amplitude of pressure perturbations generated by fast acoustic waves is adjusted by a factor of 1/1541.67, so that the maximum amplitudes

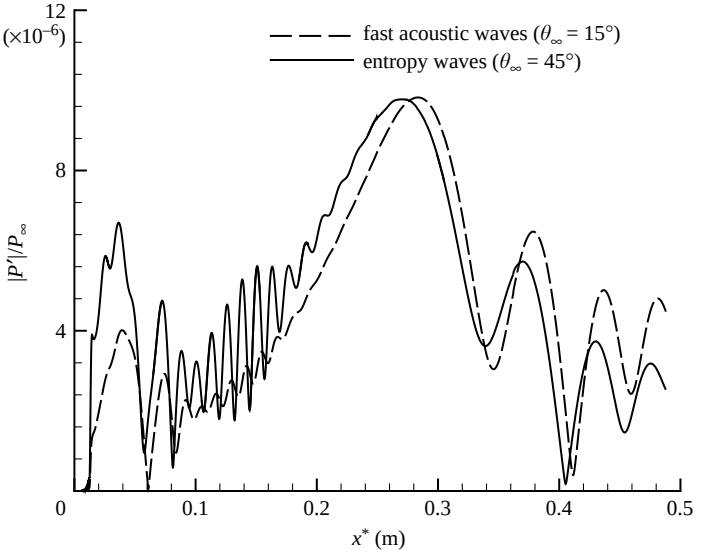

FIGURE 22. Distributions of amplitudes of boundary-layer disturbances generated by different free-stream forcing waves: —, free-stream plane entropy waves (case E.3); – – –, free-stream fast acoustic waves (case F.2) ($M_\infty = 4.5$, $F = 2.2 \times 10^{-4}$).

are the same for both cases shown in figure 22. Because receptivity is linear in our numerical studies, the adjusted result shown in figure 22 for case F.2 is equivalent to receptivity to fast acoustic waves with $\epsilon = 3.24 \times 10^{-7}$. It is obvious that there are very similar growth and decay patterns of the induced waves between the two cases shown in figure 22, which indicates that the same dominant waves are generated in boundary-layer disturbances for the two cases. The dominant components of the boundary-layer disturbances at different locations induced by fast acoustic waves have been identified in Ma & Zhong (2003*b*). Mode I waves are first generated in the leading-edge region ($x^* < 0.1$ m). The second Mack mode is subsequently generated by mode I in a later region ($0.1\,\text{m} < x^* < 0.2\,\text{m}$) by means of a resonant interaction. Still further downstream, stable mode II waves are dominant in the region of $x^* > 0.2$ m (figure 22). Through the comparison shown in figure 22, we can identify the dominant components of boundary-layer disturbances induced by free-stream entropy waves at all different locations as being the same as those induced by the free-stream fast acoustic waves.

The phase velocities of boundary-layer disturbances for case E.3 are compared with case F.2 in figure 23. In addition, the phase velocities of boundary-layer normal modes calculated by LST are also plotted in this figure for comparison. The comparison of the phase velocities of the induced boundary-layer disturbances and the corresponding LST results of the normal modes can be used to identify wave modes of the induced boundary-layer disturbances. As expected, the phase velocities of the boundary-layer disturbances for the current case of free-stream entropy waves is very close to those of mode I waves near the leading edge, while there is a good agreement between the phase velocities of the boundary-layer disturbances and those of mode II waves in the region downstream ($x^* > 0.2$ m). As discussed in Ma & Zhong (2003*b*), mode I and mode II waves are generated and amplified in the receptivity simulations due to the resonant interaction between the generated fast acoustic waves behind the shock and the two boundary-layer wave modes. Although mode I and mode II waves are

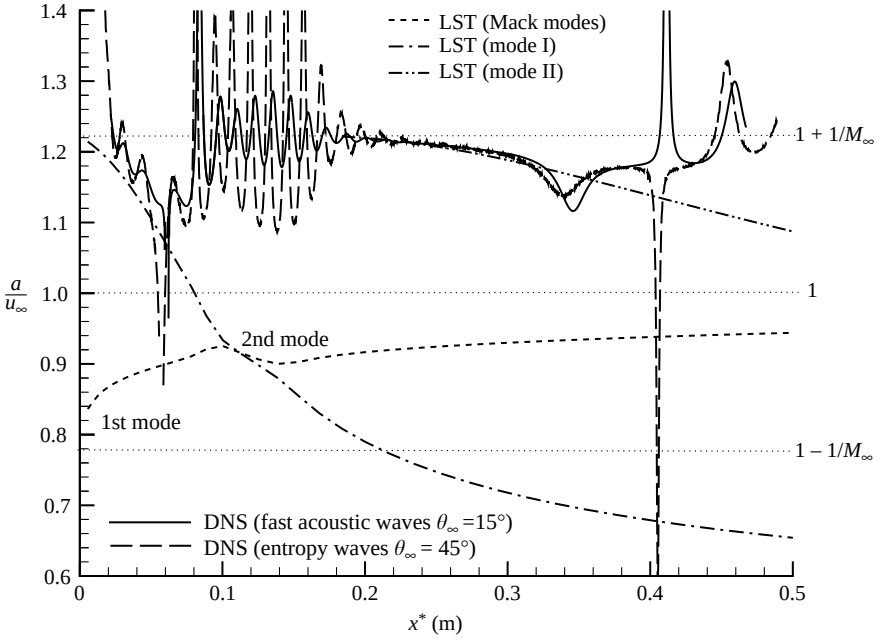

FIGURE 23. Distribution of phase velocities of boundary-layer disturbances due to free-stream plane entropy waves (case E.3) and comparison with LST results ($M_\infty = 4.5$, $F = 2.2 \times 10^{-4}$ and $\theta_\infty = 45°$).

predicted to be stable by the LST, their magnitudes grow because of the resonant interactions. The phase velocities of mode I (or mode II) decrease during their propagation downstream. As a result, the mode I (or mode II) waves decay owing to their inherent stable properties, when their phase velocities decrease to a value where there is no more resonant interaction between the mode I (or mode II) waves and fast acoustic waves. Before mode I waves die out, they are synchronized with the Mack mode at their mutual wave synchronization point located at $x^* = 0.11$ m. According to our previous study (figure 7 in Ma & Zhong 2003*a*), both the first Mack-mode waves and mode I waves have almost the same profiles of disturbance structure across the boundary layer at the synchronization point. As a result, mode I waves convert to the Mack-mode waves in the synchronization region. Although the second-mode waves are amplified owing to inherent instability, there are strong oscillations in the phase velocity curve (figure 23) and the pressure perturbations (figure 22) in the middle region owing to a modulation between the Mack mode waves and other waves, such as acoustic waves and mode II waves. From the comparison of the receptivity to free-stream fast acoustic waves in figure 23, it is clear that the boundary-layer disturbances in the current case of free-stream entropy waves are generated by fast acoustic waves behind the shock.

7.2. *Free-stream entropy waves with* $F = 1.6 \times 10^{-4}$ *and* $\theta_\infty = 45°$ (*case E.7*)

In figure 24, the induced pressure perturbations on the wall surface for case E.7 are compared with case F.3. Since linear receptivity is simulated here, the amplitude of pressure perturbations generated by fast acoustic waves is rescaled by a factor of 1/1250 in figure 24 in order to compare with the results of the receptivity to free-stream entropy waves. It should be noted that the amplitudes are adjusted so that

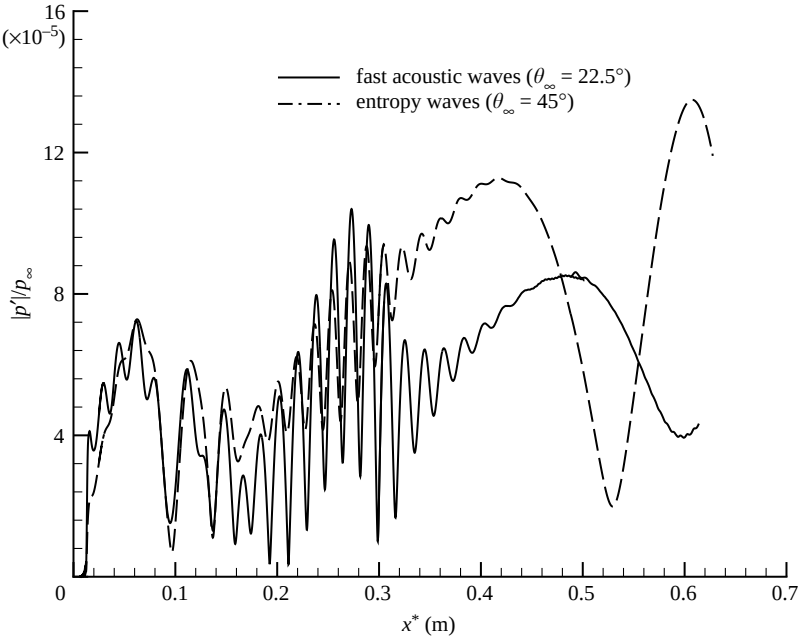

FIGURE 24. Comparison of boundary-layer disturbances generated by free-stream plane entropy waves (case E.7) with those generated by free-stream acoustic waves (case F.3) ($M_\infty = 4.5$, $F = 1.6 \times 10^{-4}$).

the local peak values are the same as in the pressure perturbations at $x^* = 0.062$ m in figure 24. Overall, figure 24 shows that the growth and decay of the wave patterns of the two cases are very similar. For case F.3, the wave angles of the transmitted fast acoustic waves behind the shock decrease from $\theta_\infty = 26.2°$ near the leading edge to $\theta_\infty = 23.4°$ at the exit based on the linear theory. On the other hand, the wave angles of the generated acoustic waves (θ_2) by free-stream entropy waves are predicted to be between 24.9° (at the inlet) and 15.7° (at the exit). Because the wave angles of the generated fast acoustic waves behind the shock for the two cases are close to each other in the region near the leading edge, figure 24 shows that the wave patterns of the two cases in the upstream region are very similar. The wave patterns of the two cases differ in the downstream region because wave angles of the transmitted acoustic waves alter more.

Because the dominant components of the boundary-layer disturbances induced by free-stream fast acoustic waves have been identified in Ma & Zhong (2003*b*), the dominant waves inside the boundary layer induced by free-stream entropy waves shown in figure 24 can be identified by comparing with the receptivity results for the case of free-stream fast acoustic waves. Similar to the case of free-stream fast acoustic waves, it can be shown that the dominant wave modes shown in figure 24 are mode I waves in the leading-edge region ($x^* < 0.19$ m), second-mode waves in the middle region ($0.19\text{ m} < x^* < 0.38$ m), and mode II waves in downstream region downstream ($x^* > 0.38$ m). Again, the oscillations of the perturbation amplitudes in the second-mode region are a result of a wave modulation among the second mode, mode II waves and other waves.

The identification of the dominant waves inside the boundary layer induced by free-stream entropy waves is confirmed by comparing the phase velocities of the induced

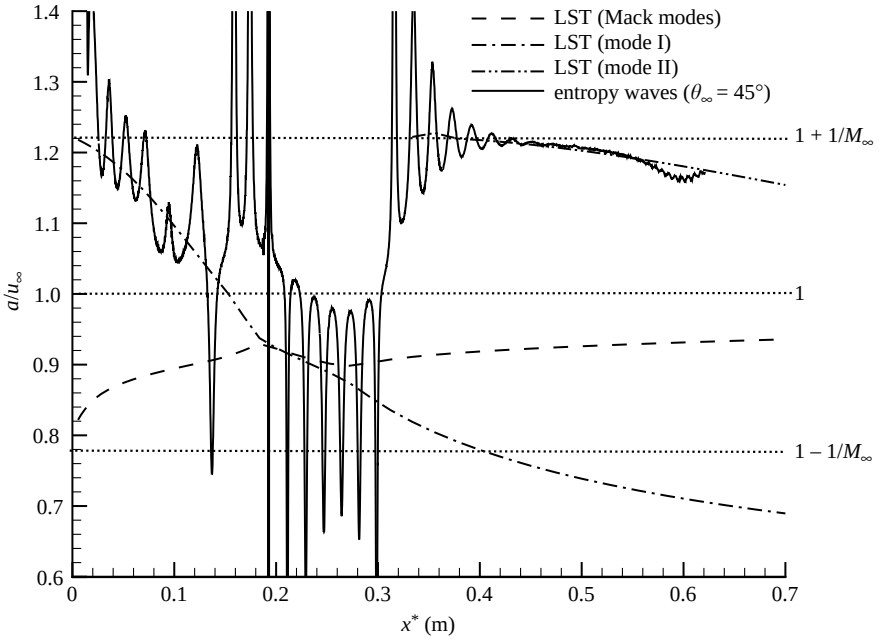

FIGURE 25. Distribution of phase velocities of boundary-layer disturbances due to free-stream plane entropy waves (case E.7) and comparison with LST results ($M_\infty = 4.5$, $F = 1.6 \times 10^{-4}$ and $\theta_\infty = 45°$).

boundary-layer disturbances with those of the boundary-layer normal modes obtained by LST calculations. Figure 25 shows such comparison of the phase velocities. As expected, the phase velocities of the induced boundary-layer disturbances are close to those of mode I waves near the leading edge, while there is a good agreement between the phase velocities of boundary-layer disturbances and mode II waves in the region downstream ($x^* > 0.38$ m). In the middle region ($0.19\,\text{m} < x^* < 0.38\,\text{m}$), there are strong oscillations in the phase velocities of boundary-layer disturbances due to a modulation between Mack mode waves and other waves, such as acoustic waves and mode II waves. At the beginning of the generation of the second mode near the location of $x^* = 0.17$ m, the initial amplitude of the second-mode waves are weak compared with other components of modulation. The oscillations of the phase velocity curve are around the phase velocity of the fast acoustic waves. After the generation of the second mode from the mode I waves, the second mode is strongly amplified because it is unstable. As a result, as shown in figure 25, the oscillation centre of phase the velocity curve is close to the phase velocities of the second mode. The second mode waves begin to decay after passing their branch II neutral stability point. In the region downstream of $x^* > 0.3$ m, the amplitudes of the second-mode waves are so weak that the oscillation centre of the phase velocity curve moves back to phase velocities of the fast acoustic waves and the mode II waves. The dominant boundary-layer mode in a different region is further confirmed by comparing fluctuation profiles with the LST results, which is not shown here owing to space limitations.

7.3. *Free-stream entropy waves at frequency* $F = 1.6 \times 10^{-4}$ *at different incident wave angles*

Figure 26 compares the amplitudes of pressure perturbations along the wall surface for cases E.5 to E.8. It shows that the wave patterns of the induced waves change

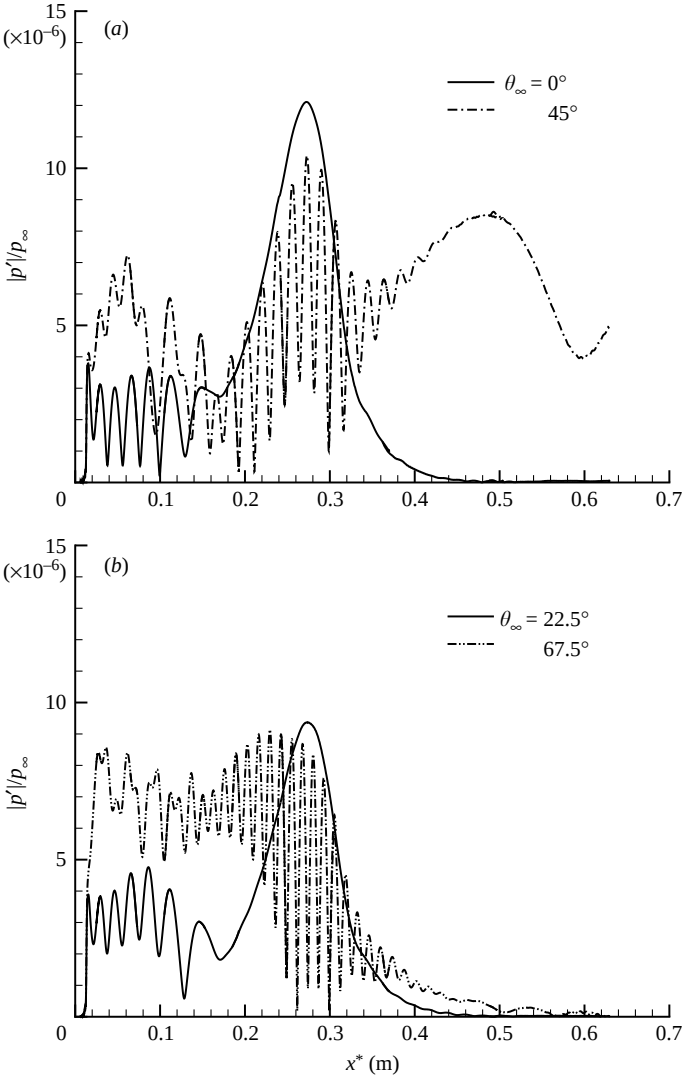

FIGURE 26. Distributions of pressure perturbations on the wall due to free-stream plane entropy waves for cases E.5 to E.8 ($M_\infty = 4.5$, $F = 1.6 \times 10^{-4}$).

dramatically when the incident wave angles change. In other words, there is a strong effect of the incident wave angles. However, after ignoring high spatial frequency oscillations due to wave modulation, the overall trend of growth and decay in wave patterns induced by free-stream entropy waves are very similar for different incident angles except that boundary-layer disturbances are strongly amplified in the region downstream $x^* > 0.4$ m for case E.7 (see figure 26). The amplified boundary-layer disturbances are identified as mode II waves by comparing the phase velocities and fluctuation profiles with the LST results. As discussed in § 5, boundary-layer disturbances are strongly affected by the impingement of fast acoustic waves on the wall surface for the case E.8 (figure 6). As a result, the development of boundary-layer disturbances for this case looks different from the other three cases with smaller incident wave angles. Specifically, the development of mode I waves for case E.8

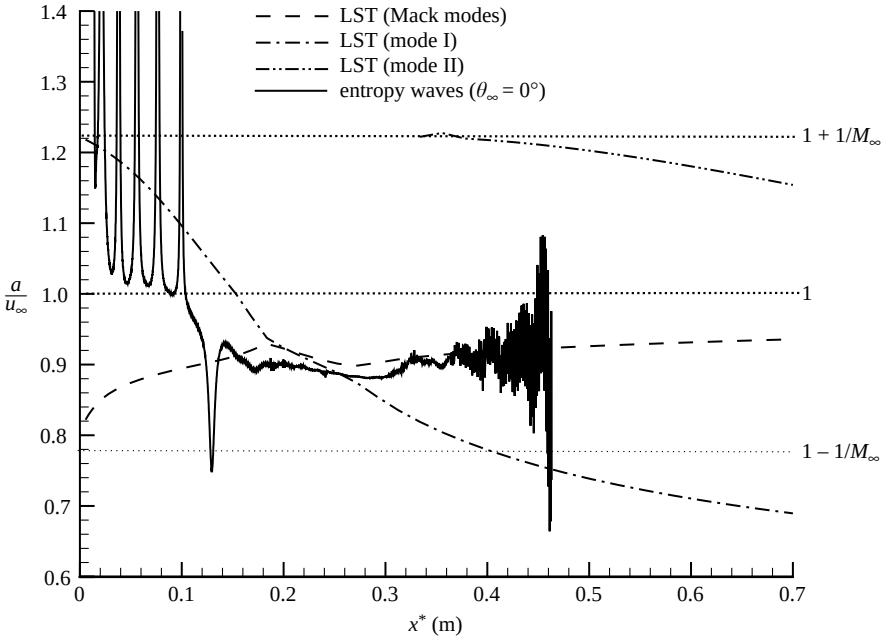

FIGURE 27. Distribution of phase velocities of boundary-layer disturbances due to free-stream plane entropy waves (case E.5) and comparison with LST results ($M_\infty = 4.5$, $F = 1.6 \times 10^{-4}$ and $\theta_\infty = 0°$).

becomes unclear owing to the effect of the strong impingement of the fast acoustic waves. For cases E.5 and E.6, there is a clear path of the generation and growth of the second mode waves.

Figure 27 compares the phase velocities of case E.5 with those of the boundary-layer normal modes obtained by LST calculations. In the region near the leading edge ($x^* < 0.16$ m), there are strong oscillations in numerical results for the phase velocity curve centred near that of mode I waves from the LST results. Again, mode I waves are generated by forcing fast acoustic waves first. The second mode waves are generated afterward. Compared with figure 25, there is a better match between the current simulation results and the LST results for the second-mode waves. From figure 26, it shows that the second mode waves begin to grow at $x^* \approx 0.17$ m ($RF = 0.177$) for cases E.5 and E.6, which is close to the synchronization point between mode I and the second-mode waves located at $x^* = 0.2$ m from the LST results. The second-mode waves grow very rapidly before reaching the branch II neutral stability location. After passing the branch II location, boundary-layer disturbances decay very rapidly and die out in the region downstream ($x^* > 0.45$ m). From the simulation results, the second-mode branch II neutral points are located at $x^* = 0.272$ m ($RF = 0.2239$) and $x^* = 0.2745$ m ($RF = 0.2249$) for the two cases of $\theta_\infty = 0°$ and 22.5°, respectively. These values agree well with that of the LST prediction ($RF = 0.2250$). At the second-mode branch II location, the amplitudes of the pressure perturbation are 1.2×10^{-5} for case E.5 and 9.36×10^{-6} for case E.6.

The second mode waves are generated from mode I waves. It is natural to assume that stronger mode I waves can generate stronger second mode waves. Figure 26 shows that the maximum amplitude of mode I waves for case E.7 ($\theta_\infty = 45°$) is much stronger than for cases E.5 and E.6 with lower incident angles ($\theta_\infty = 0°$ or $\theta_\infty = 22.5°$). However, for case E.7, the induced second mode waves are weaker. This is because

the development of mode I waves is strongly affected by modulation with other waves inside the boundary layer, such as acoustic waves, entropy waves and vorticity waves. For different incident angles of free-stream entropy waves, the wave angles of acoustic waves, entropy waves and vorticity waves inside the boundary layer are different. Therefore, there are different modulations on mode I waves for different incident angles, which lead to slower decay of mode I waves for lower incident angles compared with the $\theta_\infty = 45^\circ$ case. The initial amplitude of the second mode waves generated by mode I waves are much stronger for lower incident angles. When the incident wave angle increases to $\theta_\infty = 45^\circ$, mode I waves decay so fast that the initial amplitude of the second mode generated by mode I waves becomes very weak and the second-mode waves becomes unclear owing to modulation with other waves. Meanwhile, there are clear mode II waves shown in the region downstream where the second mode waves become stable and die out. The mode II waves reach their peak amplitude at $x^* \approx 0.5$ m. For the case E.8 ($\theta_\infty = 67.5^\circ$), there are neither clear second-mode waves nor mode II waves in boundary-layer disturbances induced by free-stream entropy waves. Distinctive second-mode waves are absent for cases E.7 and E.8 because the initial amplitudes of the generated second mode waves from mode I waves near synchronization point between the second mode and mode I are very weak. As a result, the second mode waves are modulated by other waves during their propagation downstream. Although the second-mode waves are still amplified owing to their unstable properties, they are not the dominant component of the boundary-layer disturbances. From the previous discussions on case E.8, the wave angles for the generated fast acoustic waves behind the shock in the region with $x^* < 0.21$ m shown in figure 6 are between 62.0° and 57.7°. As a result, there is a strong impingement of the generated fast acoustic waves on the wall surface, which leads to strong pressure perturbations near the leading edge. Meanwhile, the resonant interaction between the fast acoustic waves and the mode II waves, which is the main mechanism for generation and growth of the mode II waves, becomes very weak because there is much difference in phase velocity between the generated fast acoustic waves with large wave angle and the mode II waves. Therefore, the induced mode II waves by fast acoustic waves are not strong.

7.4. *Free-stream entropy waves at frequency* $F = 2.2 \times 10^{-4}$

Cases E.1 to E.4 are compared with cases E.5 to E.8 in order to study the effect of frequency on the receptivity to free-stream entropy waves. Distributions of the amplitudes of the pressure perturbations are shown in figure 28. Compared with the results of $F = 1.6 \times 10^{-4}$, the basic shapes and trends of the amplitudes of the pressure perturbations for different frequencies with the same incident wave angle are very similar. Again, figure 28 shows clearly the generation and growth of the second mode waves for the cases E.1 and E.2 with lower incident angles. The second-mode waves are generated at about $RF = 0.182$ ($x^* = 0.095$ m) from numerical results, which is close to the value of $RF = 0.177$, for the cases of $F = 1.6 \times 10^{-4}$. The peak amplitudes of the pressure perturbation at the second-mode branch II neutral stability point ($x^* = 0.140$ m for $F = 2.2 \times 10^{-4}$ or $RF = 0.220$) are 3.44×10^{-6} for case E.1, and 2.91×10^{-6} for case E.2. At $\theta_\infty = 45^\circ$, the receptivity of mode II waves is dominant and the pressure perturbations reach a peak amplitude of 9.77×10^{-6} at $x^* = 0.272$ m ($RF = 0.301$), compared with the corresponding value of 8.6×10^{-6} at $x^* = 0.492$ m ($RF = 0.308$) for $F = 1.6 \times 10^{-4}$ with the same incident wave angle (figure 26). Again, in terms of RF, the locations of the peak amplitude of the second-mode (or mode II) waves are almost the same for both cases of different frequencies. As discussed

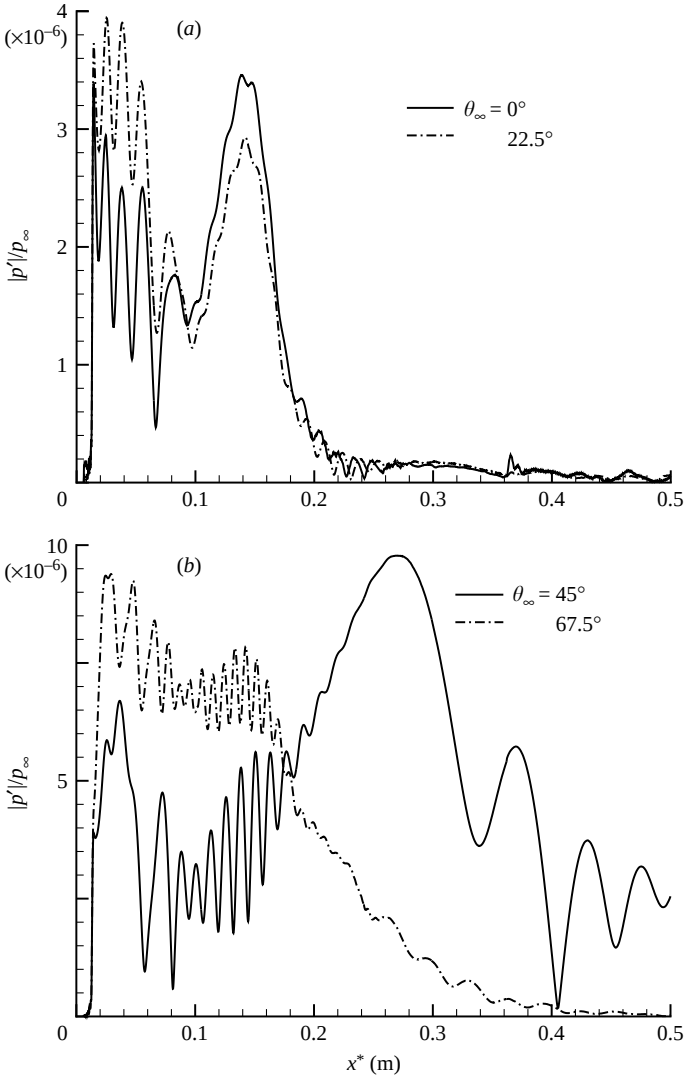

FIGURE 28. Distributions of pressure perturbations on the wall due to free-stream plane entropy waves for cases E.1 to E.4 ($M_\infty = 4.5$, $F = 2.2 \times 10^{-4}$).

before, for the case of $\theta_\infty = 67.5°$, the development of boundary-layer disturbances are strongly affected by the impingement of fast acoustic waves on the wall surface. Consequently, the induced boundary-layer disturbances are neither dominated by the second Mack mode waves nor dominated by the mode II waves.

7.5. *Response coefficients*

To quantitatively study the receptivity of the supersonic boundary layer to free-stream entropy/vorticity waves, the response coefficient is redefined as

$$K_{mode} = \frac{|p'_{mode}|}{\epsilon |p_\infty|}, \tag{20}$$

where $|p'|_{mode}$ is the maximum amplitude of pressure perturbations for a given wave mode. For the second Mack mode, this maximum value is located at the branch II

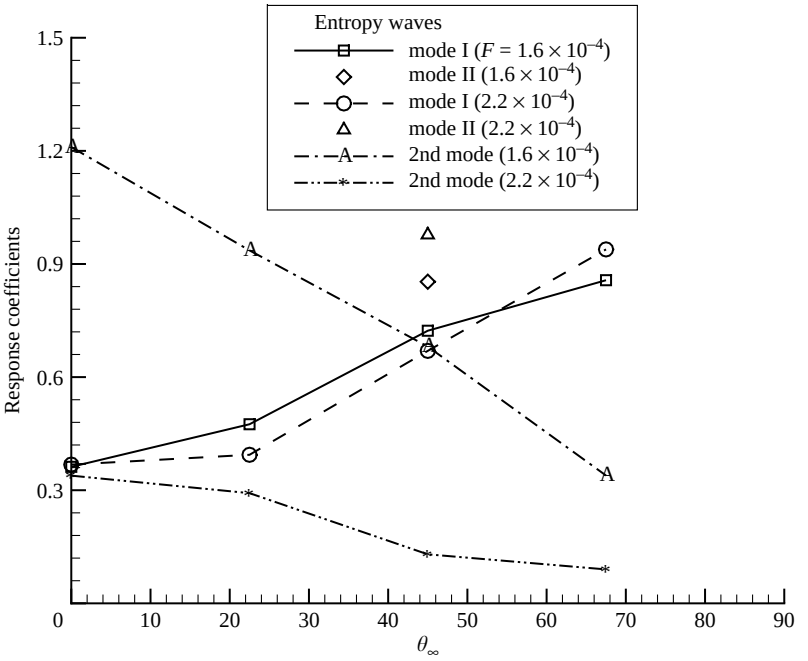

FIGURE 29. Response coefficients of the boundary-layer normal modes to free-stream entropy waves *vs.* incident wave angles for cases E.1 to E.8 ($M_\infty = 4.5$).

neutral stability point. Spatial Fourier analyses and band-pass filter windows described in Ma & Zhong (2003*b*) are used to separate the second mode from other wave modes in the simulation results. The response coefficients can be easily converted to the branch I receptivity coefficient if divided by 5.2 and 10.6 for $F = 2.2 \times 10^{-4}$ and 1.6×10^{-4}, respectively.

Response coefficients for the numerical results shown in figures 26 and 28 are calculated based on (20). Figure 29 compares the response coefficients for eight test cases of free-stream entropy waves at four different incident wave angles and two different frequencies. From figures 26 and 28, mode II waves are clearly present for cases of $\theta_\infty = 45^\circ$ only. Therefore, there are only two discrete points shown in figure 29 for the response coefficients of mode II waves with value $K_{II} = 0.84$ and $K_{II} = 0.96$ for $F = 1.6 \times 10^{-4}$ and $F = 2.2 \times 10^{-4}$, respectively. Figure 29 also shows that the response coefficients of the mode I waves at different incident wave angles are close to each other for cases of the two different frequencies, while the response coefficients of the second Mack mode are much larger at lower frequency because the second mode waves are more strongly amplified. With the increase of incident wave angles, the response coefficients of mode I waves increase owing to stronger impingement of the forcing acoustic waves on the wall surface. On the contrary, the response coefficients of the second-mode waves decrease with the increase of the incident wave angles because initial amplitudes of the second mode converted from mode I waves decrease when incident wave angles increase.

7.6. *Resonant interaction between entropy waves and mode I*

As shown by the preceding discussions on the receptivity to free-stream entropy waves at frequencies $F = 2.2 \times 10^{-4}$ and $F = 1.6 \times 10^{-4}$ with different incident wave

angles, boundary-layer disturbances are mainly induced by fast acoustic waves, which are generated at the oblique shock by the interactions between free-stream entropy waves and the shock. Meanwhile, the interactions between free-stream entropy waves and the shock also generated strong transmitted entropy waves behind the shock. Based on Fedorov & Khokhlov (2001)'s theoretical prediction, mode I waves can be excited directly by entropy waves near the synchronization point between entropy waves and mode I waves. From figures 23, 25 and 27, the synchronization points between entropy waves and mode I are located at $x^* = 0.08052\,\mathrm{m}$ (or $R = 761.4$ and $RF = 0.1675$) and $x^* = 0.1532\,\mathrm{m}$ (or $R = 1050.1$ and $RF = 0.1680$) for frequencies $F = 2.2 \times 10^{-4}$ and $F = 1.6 \times 10^{-4}$, respectively. Therefore, the synchronization points between the entropy waves and mode I waves in term of RF are almost a constant with value equal to 0.168 for these two different frequencies. From eight test cases shown in figures 26 and 28, for receptivity to free-stream entropy waves, mode I waves are generated by fast acoustic waves in the region upstream of the synchronization point between entropy waves and mode I waves. If mode I can be excited directly by the entropy waves, the amplitudes of the mode I waves should be amplified by resonant interactions between entropy waves and mode I waves in the vicinity of the synchronization point. Therefore, resonant interaction between entropy waves and mode I waves can be detected from the numerical results by the existence of amplifications of mode I waves near the synchronization point.

In order to observe the existence of a resonant interaction between mode I waves and the entropy waves, the region of generation and development of mode I waves shown in figures 26 and 28 is enlarged and redrawn in figure 30. For both frequencies, there is no significant amplification of boundary-layer disturbances shown near the synchronization points between entropy waves and mode I waves. From our previous study on the resonant interaction between fast acoustic waves and mode I waves presented in Ma & Zhong (2003*b*), the resonant interaction depends on the incident wave angles. However, there is no consistent growth in amplitudes of mode I waves in the vicinity of the synchronization point between mode I waves and entropy waves for different frequencies and different incident wave angles. In other words, there is no clear evidence in the numerical solutions to show that there exists strong resonant interaction between the mode I waves and the entropy waves. The lack of strong resonant interaction can be explained by the phase velocity curves shown in figures 23, 25 and 27. It shows in these three figures that there are resonant interactions between the mode I (or mode II) waves and the fast acoustic waves because the angle between the phase velocity curves of mode I (or mode II) and the fast acoustic waves are small near the initial location of the mode I (or mode II) waves. Therefore, there is a certain local region where phase velocities of the mode I (or mode II) waves and the fast acoustic waves are close to each other, which leads to a resonant interaction. However, for the mode I waves and the entropy waves, although there is synchronization point between the mode I waves and the entropy waves, the range of resonant interaction between the mode I waves and the entropy waves is much smaller than in the cases of fast acoustic waves.

8. Receptivity to planar free-stream vorticity waves

In this section, supersonic boundary-layer receptivity to planar free-stream vorticity waves with different frequencies and different incident wave angles (cases V.1 to V.8) are studied by numerical simulation.

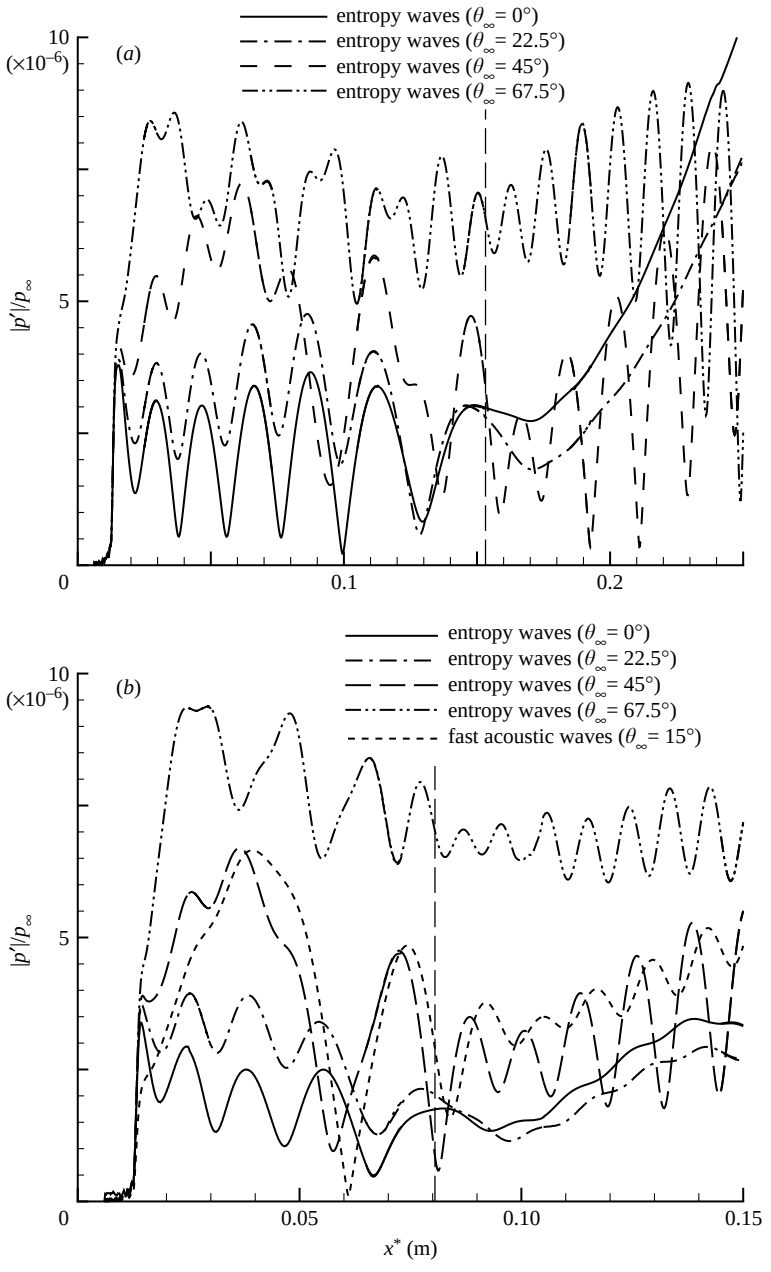

FIGURE 30. Generation and development of mode I waves near the leading edge for frequency (*a*) $F = 1.6 \times 10^{-4}$ (cases E.5 to E.8) and (*b*) $F = 2.2 \times 10^{-4}$ (cases E.1 to E.4). Location of synchronization point between entropy waves and mode I waves is marked by long dash line in each plot ($x^* = 0.1532$ m for $F = 1.6 \times 10^{-4}$ and $x^* = 0.08052$ m for $F = 2.2 \times 10^{-4}$).

8.1. *Free-stream vorticity waves at frequency* $F = 1.6 \times 10^{-4}$

As discussed in previous sections, the wave angles of the acoustic waves generated behind the shock by free-stream vorticity waves are the same as those generated by free-stream entropy waves if the incident wave angles are the same, although the amplitudes of the fast acoustic waves are different. Figure 31 compares the amplitudes

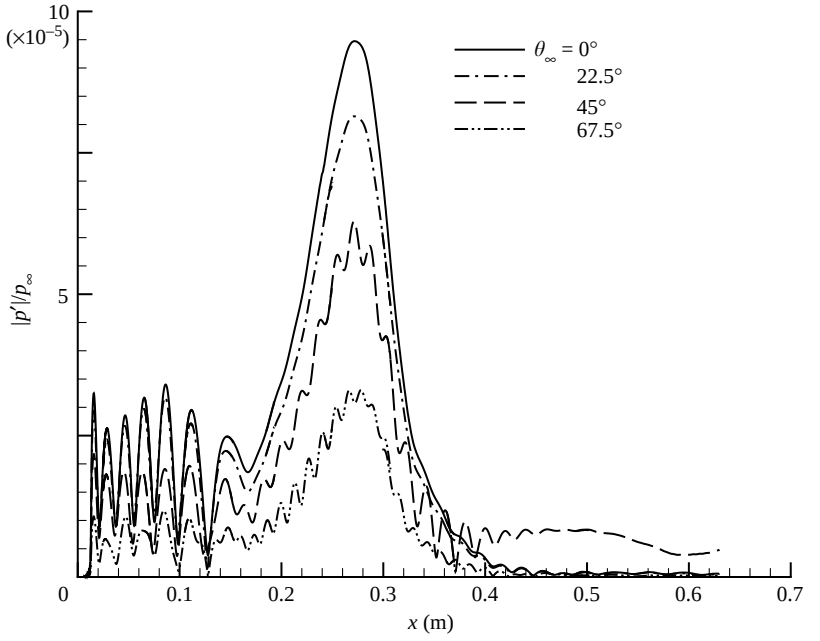

FIGURE 31. Distributions of pressure perturbations on the wall due to free-stream plane vorticity waves for cases V.5 to V.8 ($M_\infty = 4.5$, $F = 1.6 \times 10^{-4}$).

of pressure perturbations along the wall surface induced by free-stream vorticity waves for cases V.5 to V.8. It shows that there is significant growth of pressure perturbations in the region of $0.175\,\mathrm{m} < x^* < 0.272\,\mathrm{m}$. The dominant waves are identified as second mode by comparing fluctuation profiles and phase velocities with the LST results. Unlike the cases of receptivity to free-stream entropy waves, dominant second-mode waves are generated for all four cases. This figure shows that 'clean' second mode waves are generated in the region of $0.19\,\mathrm{m} < x^* < 0.38\,\mathrm{m}$ for cases V.5 and V.6, while there are some oscillations in the amplitudes of pressure perturbations in the same region owing to a wave modulation between the second-mode waves and other waves for cases V.7 and V.8. At the second-mode branch II neutral stability point ($x^* = 0.272\,\mathrm{m}$ and $RF = 0.2239$), the peak amplitudes of the second-mode waves are 9.47×10^{-5}, 8.14×10^{-5}, 6.28×10^{-5} and 3.31×10^{-5} for the four cases V.5 to V.8, respectively. With increasing incident wave angles, the receptivity of the second mode to free-stream vorticity waves becomes dramatically weaker.

Figure 32 compares the amplitudes of pressure perturbations between cases E.5 and V.5. Here, the amplitudes of pressure perturbations generated by free-stream entropy waves is rescaled by a factor of 7.8 so that the maximum value of the pressure amplitudes is the same as the corresponding maximum pressure perturbation induced by free-stream vorticity waves. This figure shows that the development of boundary-layer disturbances characterized by pressure perturbations are almost identical for these two cases. Based on this observation, it appears that the same receptivity mechanisms are involved in receptivity to free-stream vorticity waves and entropy waves. The amplitudes of the generated fast acoustic waves at the shock for cases E.5 and V.5 are compared in figure 10(*b*). It shows that the amplitudes of pressure perturbations due to vorticity waves are almost twice as large as those due to free-stream entropy waves. If boundary-layer disturbances are induced only by fast

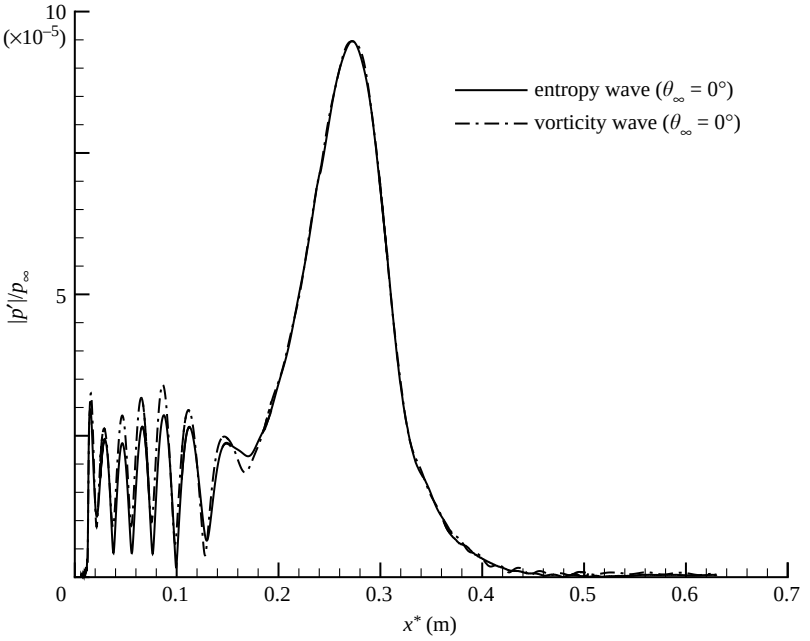

FIGURE 32. Distribution of pressure perturbations due to free-stream plane vorticity waves (case V.5) and comparison with that due to entropy waves (case E.5) ($M_\infty = 4.5$, $F = 1.6 \times 10^{-4}$ and $\theta_\infty = 0°$).

acoustic waves generated behind the shock, the amplitudes of pressure perturbations on the wall induced by free-stream vorticity waves should be nearly twice those induced by free-stream entropy waves. However, the simulation results show that the maximum amplitude of pressure perturbations on the wall induced by free-stream vorticity waves is about 7.8 times that induced by free-stream entropy waves. The unexpected stronger receptivity for the case of free-stream vorticity waves may be due to stronger interaction between boundary-layer disturbances and the vorticity waves compared to the interaction between boundary-layer disturbances and the entropy waves.

Similarly, figure 33 compares pressure perturbations on the wall between case E.7 and V.7. It shows that the same amplitudes of mode II waves are obtained in the region $x^* > 0.4$ m. This is because mode II waves are generated by resonant interactions with fast acoustic waves. More importantly, about the same amplitudes of fast acoustic waves with the same wave angles are generated behind the shock for cases E.7 and V.7 with $\theta_\infty = 45°$ from theoretical calculation, which has been shown in figure 9(*b*). However, near the leading edge, there is a stronger interaction between vorticity waves and boundary-layer disturbances compared with the case of free-stream entropy waves. As a result, the initial amplitude of the second mode waves is much stronger for vorticity waves than for free-stream entropy waves. The phase velocities of boundary-layer disturbances of V.7 are compared with those of boundary-layer normal modes obtained by LST in figure 34. The phase velocity distribution for the case of free-stream vorticity waves is very similar to that for the case E.7 as shown in figure 25. The only difference is that there are fewer oscillations in the phase velocity curve in the region of $0.19\text{ m} < x^* < 0.38\text{ m}$ for the case V.7 compared with E.7. This is because the second mode waves generated by vorticity waves are dominant in this region.

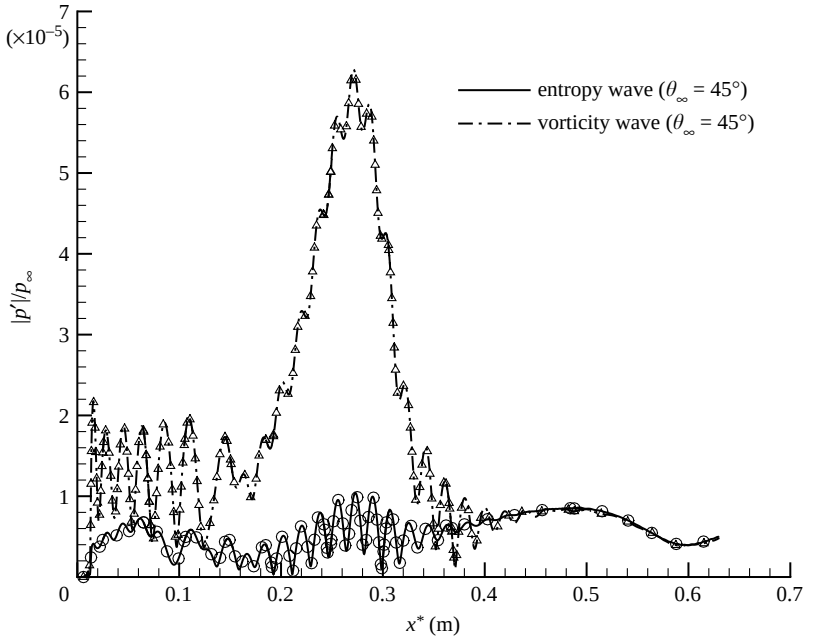

FIGURE 33. Distribution of pressure perturbations due to free-stream plane vorticity waves (case V.7) and comparison with that due to entropy waves (case E.7) ($M_\infty = 4.5$, $F = 1.6 \times 10^{-4}$ and $\theta_\infty = 45°$).

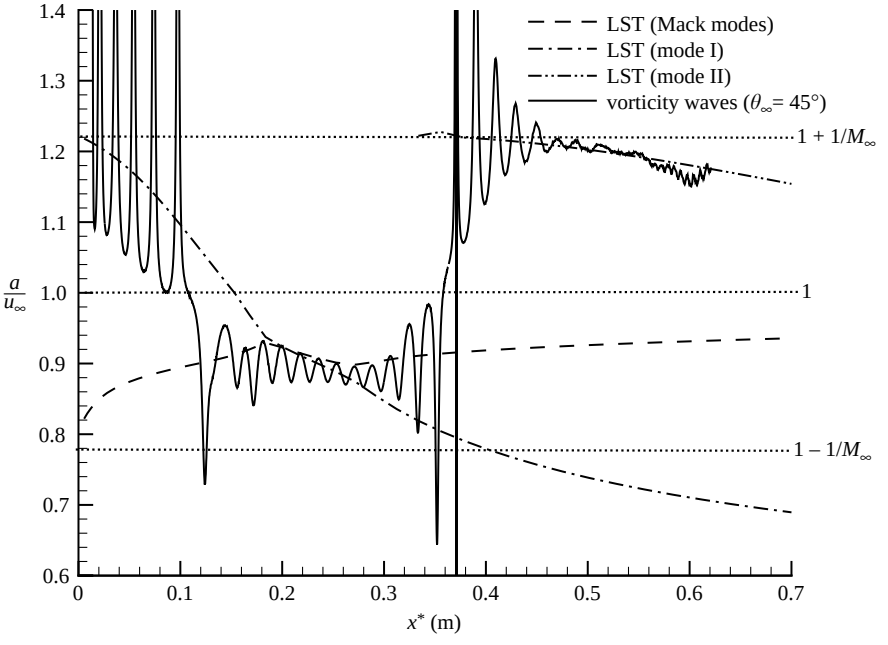

FIGURE 34. Distribution of phase velocities of boundary-layer disturbances due to free-stream plane vorticity waves (case V.7) and comparison with LST results ($M_\infty = 4.5$, $F = 1.6 \times 10^{-4}$ and $\theta_\infty = 45°$).

From the above discussions, very similar receptivity mechanisms are involved in the process of receptivity of supersonic boundary layer to free-stream vorticity and entropy waves. Specifically, in receptivity to free-stream vorticity waves, boundary-layer disturbances are mainly induced by fast acoustic waves generated at the shock by the interaction between forcing free-stream vorticity waves and the oblique shock. Therefore, the oblique shock plays a very important role in the receptivity process. In addition, there is a very strong interaction between the transmitted vorticity waves and boundary-layer mode I waves generated by fast acoustic waves. The second-mode waves are converted from mode I waves afterward. As a result, dominant second-mode waves are generated in all cases of vorticity waves of different incident wave angles studied in this section. Meanwhile, the dominant second-mode waves are only shown for lower incident wave angles ($\theta_\infty = 0^\circ$ and 22.5°) in receptivity to entropy waves.

8.2. *Free-stream vorticity waves at frequency* $F = 2.2 \times 10^{-4}$

In order to study the effects of frequency, a higher frequency of $F = 2.2 \times 10^{-4}$ was also considered. Figure 35 compares the distributions of pressure perturbations along the wall surface for cases V.1 to V.4. Again, the generation and development of boundary-layer disturbances shown in this figure are very similar to those shown in figure 31 for the frequency of $F = 1.6 \times 10^{-4}$. Dominant second-mode waves are generated for low incident angle cases V.1 and V.2, while the second mode waves are strongly modulated for the two cases V.3 and V.4 with higher incident angles. The differences between the two frequencies are the amplitudes of boundary-layer disturbances and the branch II neutral stability locations where the maximum amplitudes are reached. For the cases of $F = 2.2 \times 10^{-4}$, the peak amplitudes of the second-mode waves at branch II neutral point ($x^* = 0.140\,\mathrm{m}$ and $RF = 0.220$) are 2.46×10^{-5}, 2.06×10^{-5}, 1.68×10^{-5} and 9.65×10^{-6} for cases V.1 to V.4, respectively. Again, with the increase of incident wave angles, the receptivity of the second mode to free-stream vorticity waves decreases dramatically. In addition, for different incident wave angles at $F = 1.6 \times 10^{-4}$, the peak amplitudes of the second-mode waves are about 4 times of those of the cases of $F = 2.2 \times 10^{-4}$.

8.3. *Response coefficients for receptivity to vorticity waves*

Similar to the cases of free-stream entropy waves, (20) is used for quantitative analysis on the receptivity of the supersonic boundary layer to free-stream vorticity waves. Figure 36 compares the response coefficients induced by free-stream vorticity waves at four different incident wave angles and two different frequencies. The response coefficients are calculated according to the numerical results shown in figures 31 and 35. Figure 36 shows that the second-mode receptivity is dominant at frequency $F = 1.6 \times 10^{-4}$ with four different incident wave angles, while the receptivity of mode I is dominant for the higher frequency of $F = 2.2 \times 10^{-4}$ for all different incident wave angles. When the incident wave angles increase, the response coefficients of both mode I and the second Mack mode decrease. This trend is different from the result of the response coefficients for the cases of free-stream entropy waves shown in figure 29. Again, there are only two discrete points shown in figure 36 for the response coefficients of mode II waves with the same value $K_{II} = 0.84$ for both $F = 1.6 \times 10^{-4}$ and $F = 2.2 \times 10^{-4}$. For the second mode, the response coefficients can be easily converted to the branch I receptivity coefficient if dividing by 5.2 and 10.6 for $F = 2.2 \times 10^{-4}$ and 1.6×10^{-4}, respectively.

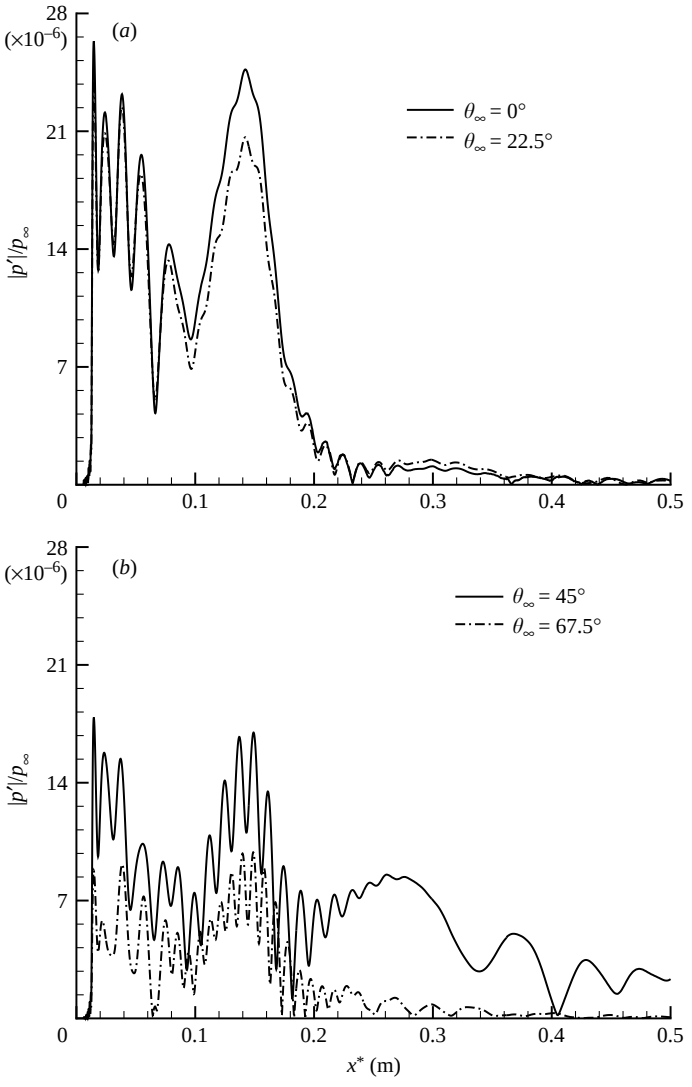

FIGURE 35. Distributions of pressure perturbations on the wall due to free-stream plane vorticity waves for cases V.1 to V.4 ($M_\infty = 4.5$, $F = 2.2 \times 10^{-4}$).

9. Discussions

The receptivity mechanisms of Mach 4.5 flow over a flat plate to free-stream slow acoustic waves, entropy waves and vorticity waves have been studied by numerical simulations. Boundary-layer normal modes induced by free-stream disturbances are identified by comparing with LST results. The results are also compared with the previously published results of the receptivity to free-stream fast acoustic waves (Ma & Zhong 2003*b*).

The results show that the receptivity to free-stream slow acoustic waves follows a different path from the receptivity to the other three types of free-stream wave. For free-stream slow acoustic waves, Mack-mode waves are generated directly by transmitted slow acoustic waves due to resonant interaction between the first-mode waves and the slow acoustic waves. The receptivity mechanism to slow acoustic waves

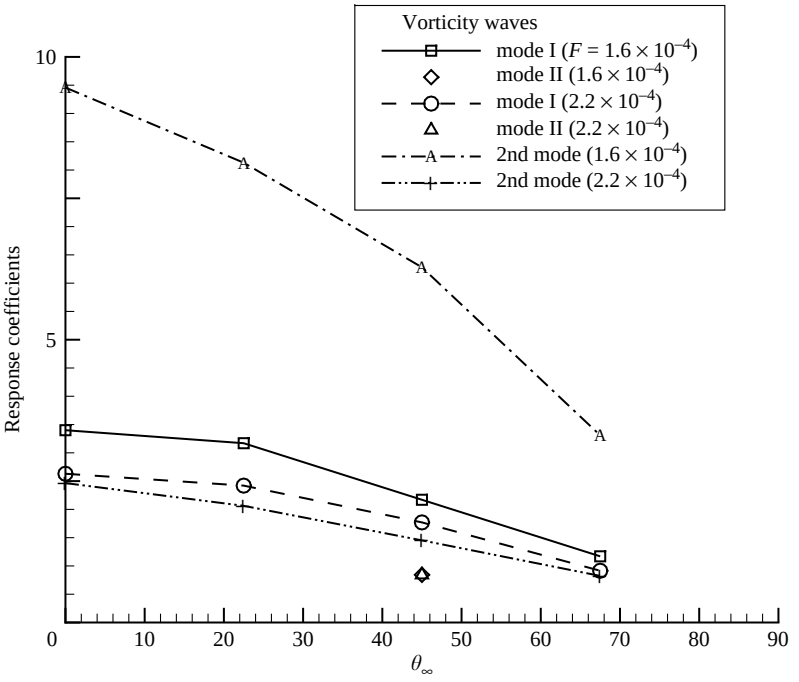

FIGURE 36. Response coefficients of the boundary-layer normal modes to free-stream vorticity waves *vs.* incident wave angles for cases V.1 to V.8 ($M_\infty = 4.5$).

is different from that to fast acoustic waves (Ma & Zhong 2003*b*). In the process of receptivity to fast acoustic waves, there are two steps of resonant interactions. First, stable mode I waves are generated by their resonant interaction with the forcing fast acoustic waves in the leading-edge region. Secondly, the second Mack mode waves are converted from stable mode I waves near their synchronization point. Because mode I waves are inherently stable, the amplitudes of mode I waves are significantly reduced before reaching their resonant interaction point with the second mode. Consequently, for free-stream fast and slow acoustic waves with incident wave angles smaller than 45°, the second-mode receptivity to free-stream slow acoustic waves are several times stronger than that to free-stream fast acoustic waves.

On the other hand, the current study shows that the receptivity of the supersonic boundary layer to free-stream entropy and vorticity waves is essentially similar to that to free-stream fast acoustic waves. In other words, for these three types of free-stream waves, the second mode waves in the boundary layer are generated by the two-step resonant interaction process involving the stable mode I waves. This is because fast acoustic waves are generated behind the shock. The generated fast acoustic waves propagate downstream, enter the boundary layer, and excite boundary-layer wave modes. Therefore, the interaction between the oblique shock and free-stream entropy/vorticity waves plays a very important role in receptivity. Numerical simulation on the generated fast acoustic waves at the oblique shock is compared with McKenzie & Westphal's (1968) theoretical results on linear interaction between free-stream disturbances and an oblique shock. Good agreement is obtained in both the wave angles and amplitudes of the generated fast acoustic waves. McKenzie & Westphal's linear theory is also used to analyse the receptivity mechanism of entropy waves and vorticity waves. It is found that the receptivity to free-stream

entropy/vorticity waves is mainly through the fast acoustic waves generated behind the oblique shock. The entropy/vorticity waves first generate fast acoustic waves from their interaction with the shock. In turn, the generated fast acoustic waves induce boundary-layer disturbances through the same receptivity path as that of the free-stream fast acoustic waves. The numerical results show that there is a significant effect on the development of mode I waves from its modulation with other wave components inside the boundary layer, such as acoustic, entropy and vorticity waves. However, there is no clear evidence to show that there exists strong direct resonant interaction between the mode I waves and the forcing entropy/vorticity waves, which is different from Fedorov & Khokhlov (2001)'s theoretical prediction on excitation of mode I waves by entropy/vorticity waves near their synchronization point.

The effects of incident wave angles on the receptivity are also studied. It is found that the second-mode response coefficients always decrease with increasing incident wave angles. In receptivity to free-stream entropy waves, the response coefficients of mode I waves increase with increasing incident wave angles owing to the impingement and reflection of the fast acoustic waves on the wall. In the receptivity to free-stream vorticity waves, both the mode I and the second mode waves become weaker with increasing incident wave angles. Numerical results also show that there is not much effect on the receptivity of mode I waves from the change of frequencies, while there is a significant increase in the response coefficients of the second mode for lower frequency in receptivity to different types of free-stream disturbance.

This research was supported by the Air Force Office of Scientific Research, USAF, under AFOSR Grant F49620-00-1-0101. The support of the programme manager, Dr John Schmisseur, is greatly appreciated. The views and conclusions contained herein are those of the authors and should not be interpreted as necessarily representing the official policies or endorsements either expressed or implied, of the Air Force Office of Scientific Research or the US Government.

REFERENCES

Anyiwo, J. C. & Bushnell, D. M. 1982 Turbulence amplification in shock-wave boundary-layer interaction. *AIAA J.* **20**, 893–899.

Fedorov, A. V. 1997 Laminar turbulent transition in a hypersonic boundary layer: receptivity and instability pre-history. *Final Rep.* NASA-N97-29589.

Fedorov, A. V. & Khokhlov, A. P. 2001 Prehistory of instability in a hypersonic boundary layer. *Theoret. Comput. Fluid Dyn.* **14**, 359–375.

Fedorov, A. V. & Khokhlov, A. P. 2002 Receptivity of hypersonic boundary layer to wall disturbances. *Theoret. Comput. Fluid Dyn.* **15**, 231–254.

Fedorov, A. V. & Tumin, A. 2001 Initial-value problem for hypersonic boundary layer flows. *AIAA Paper 2001-2780.*

Herbert, Th. 1996 Progress in applied transition analysis. *AIAA Paper 96-1993.*

Herbert, Th. & Morkovin, M. V. 1979 Dialogue on progress and issues in stability and transition research. In *Laminar-Turbulent Transition, IUTAM Symp. Stuttgart, Germany* (ed. R. Eppler & H. Fasel), pp. 47–72. Springer.

Kendall, J. M. 1975 Wind tunnel experiments relating to supersonic and hypersonic boundary-layer transition. *AIAA J.* **13**, 290–299.

Ma, Y. & Zhong, X. 2001 Numerical simulation of receptivity and stability of nonequilibrium reacting hypersonic boundary layers. *AIAA Paper* 2001-0892.

Ma, Y. & Zhong, X. 2003*a* Receptivity of a supersonic boundary layer over a flat plate. Part 1. Wave structures and interactions. *J. Fluid Mech.* **488**, 31–78.

Ma, Y. & Zhong, X. 2003*b* Receptivity of a supersonic boundary layer over a flat plate. Part 2. Receptivity to free-stream sound. *J. Fluid Mech.* **488**, 79–121.

McKenzie, J. F. & Westphal, K. O. 1968 Interaction of linear waves with oblique shock waves. *Phys. Fluids* **11**, 2350–2362.

Maslov, A. A., Shiplyuk, A. N., Sidorenko, A. & Arnal, D. 2001 Leading-edge receptivity of a hypersonic boundary layer on a flat plate. *J. Fluid Mech.* **426**, 73–94.

Morkovin, M. V. 1969 On the many faces of transition. In *Viscous Drag Reduction* (ed. C. S. Wells), pp. 1–31. Plenum.

Morkovin, M. V. & Reshotko, E. 1989 Dialogue on progress and issues in stability and transition research. In *Laminar–Turbulent Transition, IUTAM Symp. Toulouse, France* (ed. D. Arnal & R. Michel). Springer.

Nishioka, M. & Morkovin, M. V. 1986 Boundary-layer receptivity to unsteady pressure-gradients – experiments and overview. *J. Fluid Mech.* **171**, 219–261.

Pruett, C. D. & Zang, T. A. 1995 On simulation and analysis of instability and transition in high-speed boundary-layer flows. *Comput. Syst. Engng* **6**, 563–575.

Reshotko, E. 1984 Environment and receptivity. *AGARD Rep. 709*.

Reshotko, E. 1994 Boundary layer instability, transition and control. *AIAA Paper* 94-0001.

Ribner, H. S. 1954 Convection of a pattern of vorticity through a shock wave. *NACA TR* 1164.

Saric, W. S., Reed, H. L. & Kerschen, E. J. 2002 Boundary-layer receptivity to free-stream disturbances. *Annu. Rev. Fluid Mech.* **34**, 291–319.

Zhong, X. 1998 High-order finite-difference schemes for numerical simulation of hypersonic boundary-layer transition. *J. Comput. Phys.* **144**, 662–709.

Zhong, X. 2001 Leading-edge receptivity to free-stream disturbance waves for hypersonic flow over a parabola. *J. Fluid Mech.* **441**, 315–367.